

RICE UNIVERSITY

**Negative Interference in Systems of Coupled  
Kinesin: A Study of Self-Assembling Complexes  
With Defined Structure**

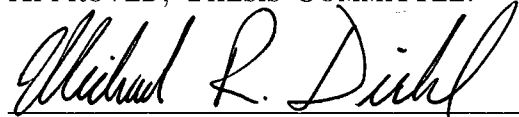
by

**Arthur Russell Rogers**

A THESIS SUBMITTED  
IN PARTIAL FULFILLMENT OF THE  
REQUIREMENTS FOR THE DEGREE

**Doctor of Philosophy**

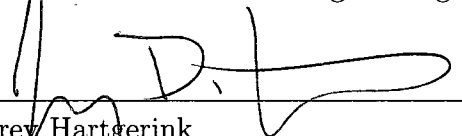
APPROVED, THESIS COMMITTEE:



Michael R. Diehl, Chair  
Assistant Professor of Bioengineering and  
Chemistry



Robert Raphael  
Associate Professor of Bioengineering



Jeffrey Hartgerink  
Associate Professor of Chemistry and  
Bioengineering

Houston, Texas

April, 2010

UMI Number: 3421336

All rights reserved

**INFORMATION TO ALL USERS**

The quality of this reproduction is dependent upon the quality of the copy submitted.

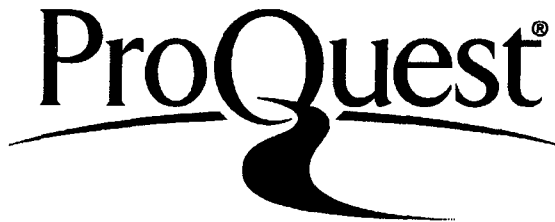
In the unlikely event that the author did not send a complete manuscript and there are missing pages, these will be noted. Also, if material had to be removed, a note will indicate the deletion.



UMI 3421336

Copyright 2010 by ProQuest LLC.

All rights reserved. This edition of the work is protected against unauthorized copying under Title 17, United States Code.



ProQuest LLC  
789 East Eisenhower Parkway  
P.O. Box 1346  
Ann Arbor, MI 48106-1346

## ABSTRACT

### Negative Interference in Systems of Coupled Kinesin: A Study of Self-Assembling Complexes With Defined Structure

by

Arthur Russell Rogers

Intracellular transport is a crucial process that requires the work of motor proteins to distribute necessary cargos. Many times the motors must move over long distances and against high opposing forces than those generated by single motors. To accomplish this task motors appear to act in teams, as suggested by experiments that show enhanced force production and extended travel lengths. Many motors have been characterized individually, but experiments to study their collective mechanics rely on non-specific groupings where the copy number and geometric arrangement are not explicitly known. In order to resolve the true extent to which each motor contributes enhanced transport properties, a system must be developed that precisely controls the number of motors that are studied. Within this work, a convergent self-assembly approach is presented that allows structurally-defined complexes of kinesin-1 to be created. This approach also provides synthetic control over intermotor spacing and the elasticity of the mechanical motor linkages to rigorously characterize the effects of system structure on the interactions of exactly two motors. This synthetic coupled motor system was then used to examine the extent to which motor grouping enhances the transport properties of cargos. It was determined that the average velocity of coupled kinesin proteins was statistically indistinguishable from that of the

single motor, while the average run lengths of the two-motor system were slightly longer ( $\approx 2X$ ), but less than estimated for a system of non-interacting motors ( $\approx 4X$ ). This study concludes that, under low loads, intermotor strain in coupled kinesin proteins increases the rate of motor detachment from the microtubule and decreases the rate at which additional motors rebind. The presence of negative interference in these complexes implies that groupings of kinesins preferentially travel in a single motor-attachment state, and that only a subset of cargo-bound motors are used during transport.

# Contents

Abstract	ii
List of Illustrations	vi
List of Tables	viii
<b>1 Introduction</b>	<b>1</b>
1.1 The Importance of Transport to Cellular Function . . . . .	2
1.1.1 Structure and Properties of Kinesin-1 . . . . .	4
1.1.2 Multimotor Transport . . . . .	7
1.1.3 Coupling Kinesin Proteins Together . . . . .	12
<b>2 Self-Assembling Materials for Building Coupled Enzyme Complexes</b>	<b>14</b>
2.1 Building Multiprotein Assemblies to Study Coupled Enzyme Interactions . . . . .	15
2.2 Convergent Synthesis of Protein Complexes . . . . .	16
2.2.1 Building Protein Arrays on Rigid DNA Scaffolds . . . . .	18
2.2.2 Interfacing DNA With Protein . . . . .	19
2.2.3 Forming Noncovalent Protein-Protein Connections . . . . .	19
2.2.4 Linkers of With Programmable Elastic Compliance . . . . .	20
2.2.5 Tuning the System to Study Coupled Kinesin . . . . .	21
2.3 Verifying Formation of the Multi-Protein Assembly . . . . .	23
2.4 Chapter Conclusion . . . . .	27
2.5 Methods for Building Self-Assembling Components . . . . .	28

2.5.1	Artificial Linker Protein Design and Purification . . . . .	28
2.5.2	DNA scaffold synthesis . . . . .	33
2.5.3	Creation of Kinesin Fusion Plasmids and Motor Expression . . . . .	39
<b>3</b>	<b>Negative Interference in Coupled Kinesin at Zero Load</b>	<b>51</b>
3.0.4	Preconceptions of Grouped Kinesin Behavior . . . . .	52
3.0.5	Building Coupled Kinesin Complexes . . . . .	53
3.0.6	Kinesin Motility on Surface-mounted Axonemes . . . . .	54
3.0.7	Signatures of Coupled Motor Transport . . . . .	56
3.0.8	Measurements at Limiting Concentrations of ATP . . . . .	58
3.1	Transition State Analysis of Coupled Motor Systems . . . . .	61
3.1.1	Negative Interference in Coupled Kinesin . . . . .	67
3.2	Methods to Assay Coupled Motor Activity . . . . .	68
3.2.1	Assay Conditions . . . . .	68
3.2.2	Microscopy and Data Analysis . . . . .	70
<b>4</b>	<b>Conclusion</b>	<b>71</b>
4.1	Conclusion . . . . .	71
4.2	Negative Interference: Continued Studies of the Two Motor Case . . . . .	72
4.2.1	Discrete Transition State Modeling of Coupled Motor Transport . . . . .	72
4.2.2	Coupled Motor Response to Applied Load . . . . .	74
4.3	Future Directions . . . . .	74
4.3.1	Increased Elastic Compliance . . . . .	74
4.3.2	Dynamic Motor Attachments to Cargo . . . . .	75
4.3.3	Creating Bidirectional Complexes . . . . .	76
	<b>Bibliography</b>	<b>78</b>

# Illustrations

1.1	Domain Maps of Kinesin Heavy and Light Chains . . . . .	5
1.2	Diagram of Kinesin Interaction With Microtubules and Self-inhibition . . . . .	6
2.1	Creating Binary Protein Complexes . . . . .	18
2.2	Sizing the Coupled Kinesin Complex . . . . .	23
2.3	Evidence of DNA Scaffold Influence in Optical Trapping Measurements . . . . .	25
2.4	Verification of Partial Assembly of Scaffold and DNA-Protein Conjugate . . . . .	26
2.5	Diagram of Specific Attachment Microtubule Gliding Assay . . . . .	27
2.6	Denaturing PAGE Gel of Conjugate FPLC Fractions . . . . .	34
2.7	FPLC Chromatogram of DNA-Protein Conjugate . . . . .	35
2.8	Diagram of Fully Assembled 50 nm DNA Scaffold . . . . .	41
2.9	Affinity Purification of Kinesin Construct . . . . .	45
2.10	FPLC Chromatogram of Purified Kinesin Construct . . . . .	46
3.1	Diagram of Coupled-Kinesin Assembly . . . . .	54
3.2	Single Molecule Assay Format . . . . .	55
3.3	Diagram of Axoneme Structure . . . . .	55
3.4	Representative Coupled Motor Traces . . . . .	57
3.5	Dissection of Coupled Motor Trace at High ATP . . . . .	57
3.6	Single Motor Stepping at Low ATP . . . . .	59
3.7	Coupled Motor Stepping at Low ATP . . . . .	59
3.8	Single Motor Stepping Behavior . . . . .	60

3.9	Coupled Motor Stepping Behavior . . . . .	60
3.10	Pairwise Distance Histograms for Low ATP Data . . . . .	61
3.11	Compiled Data for Single Molecule Experiments . . . . .	62
3.12	Transition State Model For Kinesin Complexes . . . . .	63
3.13	Run Length Fitting Data for Coupled Motor System . . . . .	64
4.1	Scheme Showing the Discrete Transition State Model . . . . .	73



## Tables

2.1	Table of Mechanical Values for Elastin Polypeptides . . . . .	21
2.2	Artificial Protein Subunit Sequences . . . . .	29
2.3	PCR Protocol for DNAworks . . . . .	29
2.4	Required Reagents for Denaturing Purification . . . . .	30
2.5	Required Reagents for SMCC Coupling . . . . .	32
2.6	Required Buffers for Denaturing Purification of DNA Strands . . . . .	36
2.7	Denaturing Acrylamide Gel Protocol . . . . .	36
2.8	Protocol for Phosphorylation Reaction . . . . .	38
2.9	Protocol for DNA Annealing Reaction . . . . .	39
2.10	Physical Constants of 50 nm Scaffold Constituent Oligonucleotides . . . . .	40
2.11	Oligonucleotid Sequences for the 50 nm Scaffold . . . . .	40
2.12	Required Buffers for Expression . . . . .	43
2.13	Protocol for Non-Denaturing PAGE . . . . .	47
2.14	Required Reagents for Gliding Assays . . . . .	48

# Chapter 1

## Introduction

### Thesis Outline

The following chapter provides an introduction to intracellular transport, discusses the current state of the field, and gives some insights into the difficulties associated with studying multiple motor transport. Chapter 2 (beginning page 14) contains an introduction to the convergent synthetic approach and the materials used to form structurally-defined coupled kinesin systems, and describes the protocols that were used to generate these materials. The initial experiments to verify complete assembly formation are also discussed. Chapter 3 (pp. 51) introduces the study of coupled motor complexes, differences in transport behavior from that of single motors, and the analysis of multiple kinesin mechanics using an existing transition state model. The final section of the chapter provides descriptions of the experimental materials and methods. The thesis conclusion (pp. 71) is supplemented with results from ongoing experiments that give new insight into the observations of negative interference between coupled kinesin introduced in chapter 3. Proposed experiments that analyze the effects of linkage compliance and cargo attachment, and the beginnings of an approach to develop artificial bidirectional assemblies are presented.

## Chapter Outline

Intracellular transport is a fundamental aspect of life. Eukaryotic cells are extremely organized and must expend energy to sort and transfer newly synthesized materials from the cell center to their final destinations. To this end, cells employ motor proteins that use ATP hydrolysis to propel cargos along cytoskeletal tracks that line its interior. Yet, there are circumstances where these motors must move over long distances, and against opposing forces higher than the measured stall forces of individual motors. Thus, motors often appear to function collectively, as suggested by experiments that show increased force production and extended travel lengths. Many classes of microtubule motors have been identified and characterized individually, but experiments to study their collective transport properties rely on non-specific arrangements of motors where copy number, intermotor spacing, and compliance of connecting linkages are unknown. In order to understand the origins of more complex transport behavior, a system must be developed in which these parameters are known and even controlled. This work presents a convergent self-assembly approach to create coupled complexes of kinesin-1 on rigid DNA scaffolds with well-defined intermotor spacing and elastic linkages of known compliance to rigorously characterize the interactions of exactly two motors.

### 1.1 The Importance of Transport to Cellular Function

Most important cargos, including crucial proteins and organelles, are manufactured at regions of the cell that are microns from their final destinations. On this scale, distance and time constraints make relying on passive diffusion to deliver cargos impossible, and in order to sustain itself, the cell must invoke active transport by a

specialized class of enzymes known as motor proteins. This group of proteins use the chemical energy from the hydrolysis of the phosphate bonds in adenosine triphosphate (ATP) to undergo global conformational changes capable of generating piconewton-scale forces to distribute essential intracellular cargos, including: organelles, such as mitochondria,<sup>1</sup> vesicles, receptors, and transmembrane proteins.<sup>2</sup>

The transport of subcellular commodities is particularly important to neuronal physiology. Neurons have cell bodies that are around 6 - 100  $\mu\text{m}$  in diameter, but have axonal projections that can extend up to a meter or more.<sup>3</sup> The unique structure of neurons has aided the identification of kinesin-1 and cytoplasmic dynein as the primary microtubule-dependent motor proteins responsible for the long-distance, fast trafficking of materials in the neuron.<sup>4,5</sup> The microtubules that these motors interact with are long protein polymers and motors are classified by their directionality with respect to microtubule polymerization. Microtubules tend to assemble faster from a point of nucleation, including organizing centers such as the centrosome, to the cell boundary, termed the 'plus-end' direction. While the terms 'minus-end' refers to the slower growing portion of the microtubule proximal to the nucleus. In this manner, kinesin is considered a plus-end directed motor and dynein is termed a minus-end directed motor.

Axons contain very little synthetic machinery; subcellular commodities must be synthesized within the cell body and then transported to the periphery.<sup>6</sup> It is also necessary to transport spent proteins and waste back to the cell body for destruction. Interruptions in the normal function of these activities, such as the a decrease in kinesin-dependent anterograde movement, leads to accumulation of organelles and

vesicles. This produces axonal swellings, which can result in a loss of synaptic activity, and eventually neuronal death. Axonal transport is the weak link in many neurodegenerative conditions including Alzheimer's disease,<sup>7</sup> amyotrophic lateral sclerosis,<sup>8</sup> and Parkinson's disease.<sup>9</sup> Recent evidence has also shown that disruption of dynein-associated retrograde transport in axons as the operative mechanism of clinical prion diseases.<sup>10</sup>

Due to the extreme length of the axon, it is unlikely that single motors with low average run lengths ( $1\ \mu\text{m}$  for kinesin) would be able to cover such distances alone. While the confined space of the axon may increase the likelihood of single motors rebinding and perpetuating travel after a dissociation event, it is speculated that motors work in coordinated teams to transport cargos to the cell boundary, and then engage a separate set of motors for the return.<sup>11</sup> Understanding the complex nature of the balance of multi-motor transport and bidirectionality, and the origins of its disruption, are paramount in the treatment and prevention of neuronal disorders. The protein motors involved must be characterized, and the principles that govern how the structural architecture of multiple motor assemblies affects their collective transport must be clearly defined.

### **1.1.1 Structure and Properties of Kinesin-1**

Kinesin-1, often referred to as conventional kinesin or KIF5B, is a member of a super family of kinesins that are microtubule-dependent transporters. It is ubiquitously expressed in eukaryotic cells, and is responsible for transit away from the nucleus.<sup>12-14</sup> Once kinesin binds cargo, it travels to the plus end of the microtubule tracks that line the cell interior. Microtubules are hollow cylindrical tubes that are made of 13

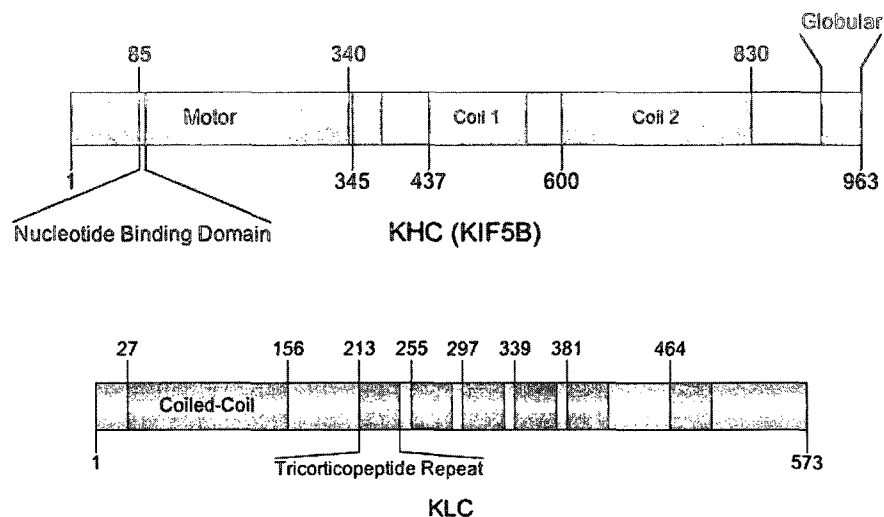


Figure 1.1 : Domain maps of kinesin heavy and light chains, highlighting identified structural features.

protofilaments assembled from  $\alpha - \beta$  tubulin heterodimers, that form a lattice of subunits separated by 4 nm.<sup>15</sup> When kinesin interacts with the microtubule, it binds exclusively to the  $\beta$ -subunit of tubulin. During kinesin's mechanical cycle, the leading head anchored to the microtubule binds ATP, swings the lagging head forward 16 nm to the next  $\beta$ -subunit (see Figure 1.2, panel A), and hydrolyzes ATP to ADP.<sup>16,17</sup> During this process the center of mass moves 8 nm, which is considered kinesin's 'step' size. Kinesin is considered a processive motor and takes hundreds of steps before dissociating from the microtubule. This total distance is referred to as a 'run length', where the average for kinesin is one micron. Electrostatic potential maps of the catalytic domains<sup>18</sup> show that the face that interacts with the microtubule is positively charged. At physiological pH, the microtubule surface is negatively charged,<sup>19</sup> and it can be assumed that electrostatic interactions play a large role in the interaction of kinesin with the microtubule.

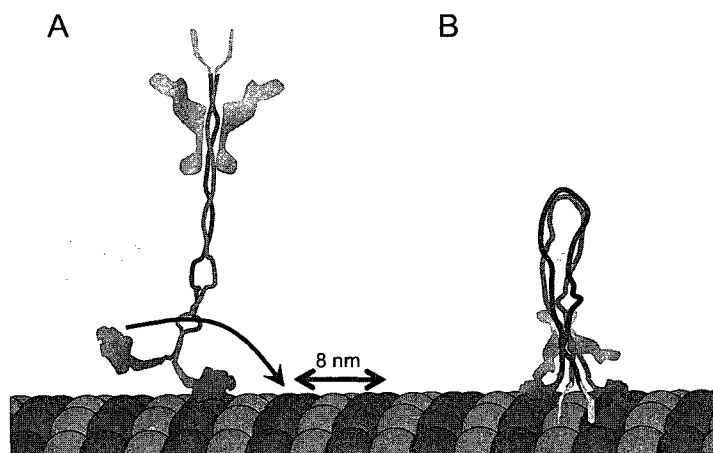


Figure 1.2 : Diagram of (A) active and (B) self-inhibited kinesin bound to microtubules. A double-headed arrow is included that shows the 8 nm separation of the microtubule subunits. (In the active state kinesin interacts with the  $\beta$ -subunits of microtubules, walking 'head-over-head'. When the motor domain binds to the microtubule, the forward head binds ATP, swinging the rear head forward 16 nm to the next  $\beta$ -subunit. Driving the center of mass forward in a step of 8 nm. (B) In the absence of cargo, it is believed that kinesin folds at the hinge region, blocking the ATP binding sites of the motor domain with the globular tail domain and the KLC.

Structurally, kinesin is a tetrameric protein consisting of two identical heavy chains, and two identical light chains. The major features in each protein are highlighted in their domain maps, see Figure 1.1. The kinesin heavy chains (KHC) are 963 amino acids (AA) in length and consist of the catalytic head domain (1-339 AA), an  $\alpha$ -helical coiled-coil stalk (340-830 AA) responsible for KHC dimerization, and a globular tail region (830-963 AA) that can interact with cargo. The hinge region between coils 1 and 2 allow the molecule to bend, bringing the head into contact with the globular tail region, which blocks the active site of the enzyme (Figure 1.2, panel B). This prevents the fruitless hydrolysis of ATP, limiting kinesin's metabolic load on the cell.<sup>20,21</sup> The kinesin light chains (KLC), each 573 AA long, associate with residues 789-813 of the KHC through a coiled-coil region (KLC 27-156 AA), and are mainly responsible for cargo recognition through a series of tetratricopeptide repeats (TPR).<sup>22-25</sup>

### 1.1.2 Multimotor Transport

While direct visualization of multiple microtubule to cargo connections, or cross-bridges, have been directly visualized with cryo-EM,<sup>13,25,26</sup> the study of native cargos has demonstrated many behaviors that clearly indicate the presence of multiple motors. In many circumstances the motors must move over long distances, and against high opposing forces. To accomplish this task motors appear to act in teams, as evidenced by experiments that show enhanced transport properties: extended travel lengths of associated cargos, increased force production, and increased velocities under applied load.



### **Increased Processivity**

Kinesin is a processive motor, and once bound to the microtubule it undergoes multiple catalytic cycles before detaching into the surrounding media.<sup>27,28</sup> While the average run-length for a single kinesin is approximately one micron, axonal transport has shown that in cells cargos can travel much longer distances (up to meters). Models in general predict that having more motors attached to the cargo that can interact with the microtubule results in longer interaction times and a greater probability of re-binding once a single motor detaches from the surface.<sup>29</sup> Bead assays that utilize non-specific adhesion of kinesin also show an increase of total travel distance with increase in motor concentration,<sup>30,31</sup> however the true number of motors engaged in transport is only estimated, and the influence of each added motor is not clear.

### **Increased Force Production**

There is also evidence for the increased force generation by teams of kinesin. Isolated kinesin proteins have been found in many studies to generate forces up to  $\approx 7$  pN, a value that is referred to as the “stall force”.<sup>32</sup> In experiments where biotinylated unilamellar vesicles were decorated with kinesin, motor groups were able to extract membrane tubules, which required a calculated force of 27pN.<sup>33</sup> The presence of super-stall forces has also been noted in optical trapping assays *in vitro*.<sup>31</sup> The measurement of the forces on endogenous lipid droplets trafficking to the cell periphery show peak values well above their gaussian average (20 pN), possibly due to transport events that engage multiple kinesin.<sup>34</sup> Under applied loads the presence of multiple engaged motors can also be inferred by the presence of multi-modal velocity histograms, suggesting that motor number varies during transport.<sup>35-37</sup> In each of these cases, the motors are distributing the force among their numbers and increasing

their ability to step under high loads.

### **Control of Cargo Transport and Motor Regulation**

While it is clear that organized groups of motors are responsible for cellular transport and organization, little is known about how structural features such as spacing, arrangement, and mechanical attachments of individual motors affects their coordinated movements. There are also many questions about how motor number and type are selected, and how they address cargos to different regions of the cell.<sup>38</sup> Altering motor number in groupings may act as a sorting mechanism to guide cargos to specific locations within the cell. For example, different populations of RNP granules may require different motor proteins to specify the site of localization.<sup>39</sup> Some microtubule tracks within cells are chemically modified, which changes the motor's affinity for certain travel paths.<sup>40</sup> For instance, isoforms of kinesin are found to bind more strongly and move with different velocities when interacting with microtubules that are detyrosinated.<sup>41</sup> This may one of the cellular mechanisms used to steer kinesin-driven cargos to particular regions of the cell. The physical obstruction of the path by microtubule associated proteins, such as tau, may also affect the intracellular cargo distribution.<sup>42</sup>

The control of motor number may also be a way to select the direction and distance that sub-cellular materials are carried. The number of engaged motors on cargos can be regulated by the expression levels of motors in cells, phosphorylation-mediated changes in cargo binding,<sup>43</sup> and heterogeneity on the surface of the microtubule (i.e. microtubule-associated proteins).<sup>31</sup> The forces between motors can also affect the binding and attachment rates of the individual motors in the assembly. For kinesin, it has been shown that the detachment rate is exponentially dependent on force, which

means the degree that forces are transmitted (the stiffness of intermotor connections) can have large impact on the motor's affinity for the microtubule.<sup>32</sup> It may be possible that accessory factors utilize this property by modulating motor connections and stimulating detachment of certain motors to control cargo movement.<sup>44</sup> In groups of oppositely-directed motors, direction may be settled through instances of tug-of-war that result in the disengagement of 'losing' motors.<sup>45</sup> In this manner, the variation of motor number attachment to cargos could determine the dominant direction of travel.

### **Asynchronous Stepping and Strain in Groups of Motors**

While coupled systems of kinesin exhibit coordinated behaviors that supersede their individual actions, observations of cargo deformation<sup>1</sup> and fractional stepping<sup>46</sup> in collective transport indicates that these movements are not always in synchrony. Furthermore, lipid tubule pulling experiments show that the force generation of motors is not necessarily additive.<sup>33</sup> It seems paradoxical that motors fight against each other when in teams, but carry cargos extreme distances and under high loads in some cases. The degree of cooperativity in kinesin systems seem to be load dependent, as shown in experiments by Gagliano *et al.* In viscous media, the velocity of bead-labeled microtubules in gliding assays is proportional to microtubule length (a measure of the number of motors bound), as opposed to standard buffers where the viscous drag against the motors is negligible ( $< 1$  pN).<sup>47</sup> For a single kinesin advancing under increasing load, its rate of stepping decreases, as described by kinesin's force-velocity relationship.<sup>48</sup> In order for a kinesin transport-dependent cargo to advance under loads higher than single motor stall forces, attached motors must bind and distribute the force equally, such that no one motor experiences forces equal to or greater than

its stall force. True load sharing requires that engaged motors keep small distances between themselves and step simultaneously.

The present study examines motors in the absence of force. In this circumstance, if one considers a linear arrangement of two motors at zero to low force, the leading motor advances rapidly in the absence of counter force. Upon binding of the lagging motor, it follows the leading motor, but given the random nature of kinesin's stepping, distance between the two can widen, resulting in the development of intermotor-forces that increase the transition to a single motor transport state. When higher forces are involved the leading motor should assume more of the load and travel at a reduced velocity. Conversely, the lagging motor experiences less of the applied load and travels at a higher velocity until it begins to inherit the applied force from the leading motor, reducing its stepping rate. With both motors experiencing sub-stall loads the cargo can progress against larger forces. Here the demand of force from the assembly may control the number of engaged motors. With both motors traveling at reduced rates, there is greater chance of stepping overlap and force equilibration between the motors. Therefore, if average forces are high, this may induce more cooperativity in the multi-motor system, but it is likely that force generation will not scale linearly (the added value of force generation per motor will not equal the single kinesin stall force), and that excess motors will still be needed.

The nature of the motor attachments are also important when considering load share between groups of motors. At close distances and high forces, stiffer linkages increase load sharing. When the leading motor advances, it assumes more of the load per step, and increases the processivity of the rear motor by decreasing its applied load. On the other hand, linkages that are more labile decrease the leading motor's force contribution per step, reducing the load relaxation benefit to the rear

motor.<sup>48</sup> Using this same principle at low loads, more compliant intermotor connections should decrease the strain coupling of the motors allowing more asynchronous steps, increasing the incidence of two motor bound states, possibly resulting in longer observed run lengths. With the inherent dependence of motor interaction on linkage compliance, the nature of the cargo attachment may define how some cargos are transported. With rigid attachments used for smaller distances with small motor number, while cargos with more flexible motor attachments on their surfaces engage more motors and travel farther. In some cases multiple motor copies might be present without design, but because of the intrinsic nature of motors like kinesin to travel as a single motor, the penalty to the cell is minimal.

### 1.1.3 Coupling Kinesin Proteins Together

The field of motor mechanics has made tremendous advances on experiments that observed the multimotor transport of intracellular particles or non-specifically adhered proteins on substrates.<sup>30,31,46,49,50</sup> Many of the motor proteins have been identified and characterized individually.<sup>16,51-53</sup> The velocities, run lengths and detachment forces obtained have been used in conjunction with mathematical modeling to determine the average number and type of motors that participate in a given assay.<sup>29,54,55</sup> There have been few studies, however, in which the number of participating motors is known with certainty, and the true contribution of each additional motor to transport remains ambiguous. Moreover, current approaches allow little synthetic control over assembly properties; in these cases, motor number, type, and arrangement on cargo are chance events. In order to understand collective motor function, it is necessary to understand how motors interact with one another, and how the geometric placement and mechanical linkages affect motile behaviors. Assemblies of motors must be

created where structural features are well characterized, and fundamental aspects of motor scaffold architecture, such as spacing between motors and the compliance of their linkages, can be determined and even tuned.

In the next chapter, a convergent self-assembly approach is used to build coupled complexes of kinesin motors on rigid DNA scaffolds, with elastic artificial protein linkers that mediate motor attachment and control compliance. This work is part of the advancement of the field, in which assemblies of motors are built from the ground up, where the type and number are well-defined.<sup>56,57</sup>

## Chapter 2

# Self-Assembling Materials for Building Coupled Enzyme Complexes

### Chapter Outline

This chapter introduces the concept of enhanced functionality in assemblies of enzymes, and describes approaches to create organized complexes to investigate these effects. Although much research has been done on single kinesin proteins, experiments that seek to recreate multimotor transport effects observed within cells rely on non-specific groupings of motors. The true number of motors that are actually engaged in these cases, and the contribution of each motor to transport, remains unclear. Currently, there is little insight into how the arrangement of individual motors on cargos and the compliance of motor attachments influence collective transport in cells. Approaches to study the interactions of coupled enzymes are hindered largely by the multiplicative inefficiency of successive labeling. With multiple labeling steps to couple proteins and include functionalities such as fluorescent dyes or anchoring chemistries to facilitate study, the final product yield becomes vanishingly small. This chapter introduces a convergent approach that utilizes self-assembling materials to create coupled motor complexes. A solution-phase capture approach was used to assemble motor proteins on a 50 nm scaffold of double-stranded DNA, through a flexible artificial protein linker. Here the materials are purified individually and combined in the final step, assuring complete labeling of constituents and preservation of

enzyme activity. The modular nature of these materials also allows for the exchange of the individual components to investigate the motor's mechanical response to structural changes, such as intermotor spacing, and linkage compliance. The final section of the chapter includes the detailed methods and protocols used to create coupled protein assemblies on rigid DNA scaffolds, and verification of their assembly through isolation of full complexes using non-denaturing polyacrylamide gel electrophoresis (PAGE), and the observations of scaffold influence on cargo motility.

## **2.1 Building Multiprotein Assemblies to Study Coupled Enzyme Interactions**

While the focus of this work is on creating artificial systems of motors, the utility of protein coupling chemistry has much broader scope. Coupled enzymatic reactions are essential to many important processes. Metabolism within cells occurs through the action of many enzymes in concert. The efficiency of multi-enzyme interactions in metabolic processes are greatly affected by variables such as enzyme concentration and distance between neighboring proteins. Many multi-unit structures, such as metabolons<sup>58</sup> and non-ribosomal peptide synthetases,<sup>59</sup> use non-covalent interactions to organize into large supramolecular assembly lines to create their final products. Many proteins also exhibit cooperativity in greater numbers. As an illustration, when multiple copies of RNA polymerase bind to the same promoter region, they prevent the pausing and backtracking events that frequently occur during single polymerase activity, resulting in dramatically increased rates of transcription.<sup>60</sup>

The assembly of enzymes into synthetic multi-protein structures is beginning to shed insight on the complex interdependent behavior of enzymes. Recently, the self-



assembly properties of DNA were utilized to examine metabolic pathways by addressing varying concentrations of metabolic enzymes within proximity of each other, creating augmented rates of product formation.<sup>61</sup> The DNA-directed assembly of proteins has also been investigated to create coupled enzyme complexes to explore the distance dependence of their coupled reaction dynamics.<sup>62</sup>

## 2.2 Convergent Synthesis of Protein Complexes

Creating coupled protein complexes presents several challenges. The proteins themselves are usually very large, with complicated tertiary and quaternary structures. Many proteins also require special conditions to maintain active folded conformations, which limits the labeling chemistries that can be used. The most common problem with creating protein arrays with multifunctional capabilities (*i.e.* fluorescent tracking, anchoring motifs, elastic linkers) is the multiplicative inefficiency of successive labeling reactions. The labeling reactions typically have low yields (on the order of 60%), which when carried through further reactions, creates even lower yields. For example, if a protein is labeled with a dye at a yield of 70%, and then covalently linked to another protein with a yield of 40%, the percent of coupled proteins labeled with dye is only 28%. At this point, the further modification of this complex suffers even more. When the proteins of study are enzymes, the conditions must also be considered to ensure enzyme viability (*e.g.*, neutral pH, low temperatures), which can detrimentally effect the rates of labeling reactions as well.

In previous experiments by Diehl *et al.*, a novel solution to this problem was presented in which the self-assembling materials were used to create multi-motor assemblies of monomeric kinesin. For this approach, heterodimeric coiled-coil forming leucine zippers created rigid motor attachments between an artificial protein scaffold

and the motor domains. This allowed the scaffold to be labeled and purified to homogeneity without concern for enzyme viability. The motors were then combined with the scaffold in solution, and the multi-motor complexes were prepared in relatively high yield. In these experiments the artificial protein was used to control the separation and elastic coupling of the motors, creating enhanced ATP hydrolysis activity, and increases in the average microtubule gliding velocity. Furthermore, it was shown that the fundamental transport mechanism was altered from monovalent binding by motors attached to elastic linkages to a bivalent ‘inchworm’ stepping process that increased the enzyme’s efficiency.<sup>63</sup>

Here, this convergent self-assembly approach is extended further to create coupled complexes of dimeric kinesin proteins on rigid DNA scaffolds. Artificial proteins covalently modified with single stranded DNA are used as an interface between the motors and the scaffold. Single strand overhangs that extend from the double stranded backbone of the DNA are hybridized with the DNA on the artificial protein, creating a mechanically flexible attachment between the motor and the DNA scaffold. Again, connections between the artificial proteins and the motor constructs utilize heterodimeric leucine zippers. The DNA backbone is extremely versatile and can be modified to include various chemistries( *e.g.*, biotin, organic dyes, etc.) depending on experimental need. While this approach has utility in creating homogenous coupled complexes, the overhang sequences can be chosen such that each attachment site is unique, and geminal complexes of proteins can be created (See Figure 2.1). This would permit the use of these materials for broader applications which study any system of interacting proteins.

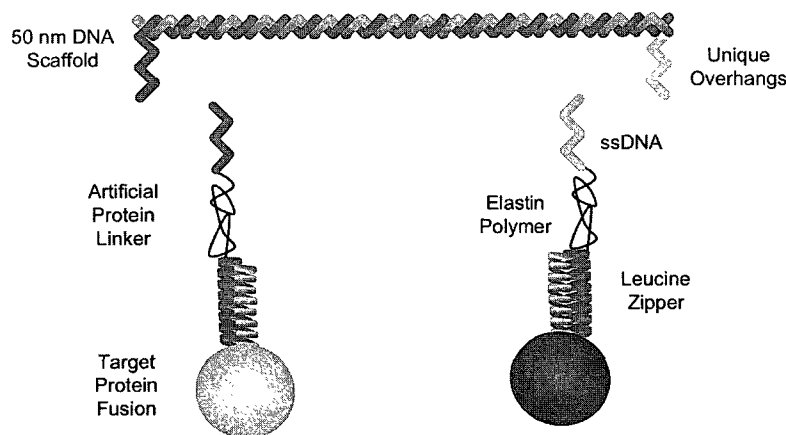


Figure 2.1 : Scheme labeling the individual components of the self-assembling protein complex. A double stranded backbone of 14 helical turns (148 base pairs) is used as a rigid scaffold is shown, with unpaired oligonucleotide extensions that can be hybridized to the covalently attached single stranded DNA on the artificial protein linker. Prior to the introduction of the DNA scaffold, the artificial proteins can be associated to the target protein through heterodimeric zipper fusions. Used in conjunction with unique overhang sequences, this approach can yield binary protein structures.

### 2.2.1 Building Protein Arrays on Rigid DNA Scaffolds

The double helix structure of DNA gives it unusual rigidity for its size. The distance over which a segment of DNA maintains direction over time (persistence length) is 50 nm. This is extremely long when compared to disordered proteins like elastin, with a persistence length of 0.4 nm. The hydrogen bonding between the bases is so reliable and specific that most forms of life utilize this molecule to store and read genetic information. When used as a nanoscale building material, DNA sequences can be programmed from the ground up, creating diverse two-<sup>64</sup> and three-dimensional architectures.<sup>65</sup> While DNA has many desirable structural properties, the custom synthesis of DNA is one of its inherent limitations. Due to the inefficiency of DNA synthesis, larger strands must be created from the successive ligations of smaller

oligonucleotides. As strands become larger, care must also be taken to avoid complementary regions that can create hairpins and other secondary structures. The non-specific interaction of DNA sequences has been thoroughly investigated, and algorithms have been created to compile sequences with minimal cross-reactions.<sup>66</sup>

### 2.2.2 Interfacing DNA With Protein

Unpaired oligonucleotides that extend from the double-stranded DNA scaffold (termed overhangs) can be hybridized with complementary sequences, and essentially function as attachment points for proteins labeled with complementary sequences of DNA. To address proteins to these overhangs on the DNA templates, cross-linking reagents can be used to covalently attach single-stranded DNA (ssDNA) to reactive amino acid side chains on the target protein (usually the amine of lysine, or the thiol of cysteine). Unfortunately, most proteins contain multiple reactive residues, and multiple DNA attachments to target proteins increase the possibility of creating uncontrolled secondary complexes. To overcome the problem of multiple labeling, an artificial protein linker was designed with a single cysteine residue to act as an intermediate between the DNA scaffold and the target protein.

### 2.2.3 Forming Noncovalent Protein-Protein Connections

To form stable connections between the target protein and the artificial protein linker, engineered heterodimeric leucine zippers were fused to both the target protein and the artificial protein linker. Leucine zippers are  $\alpha$ -helical peptides, which contain characteristic heptad repeats of the form *ABCDEFG*(see Table 2.2). For leucine zippers, the *A* and *D* positions contain leucine residues that create the hydrophobic interface between the coiled-coils. The heterodimeric zippers were developed by exchanging

residues in the *G* and *E* positions to amino acids that maintain charge at physiological pH. For  $Z_R$  these positions were substituted with positively-charged arginine residues, while the zipper denoted  $Z_E$  contains replacements with negatively-charged glutamic acid. Homodimeric complexes of the zippers result in electrostatic repulsion at the substitution points, while heterodimers participate in both hydrogen bonding and electrostatic interactions through salt bridges. Another beneficial feature of the charged residue pattern is that it preferentially aligns the zippers in a parallel arrangement. Once formed the dissociation constant is exceptionally low,  $K_d = 10^{-15}$  M, and possess weak homodimeric affinities ( $K_d = 10^{-3}$  M and  $K_d = 10^{-6}$  M for  $Z_R$ - $Z_R$  and  $Z_E$ - $Z_E$  complexes, respectively).<sup>67</sup> This strong association forms quickly, and has a low probability of partner exchange in solution. When complexed the zippers form a rigid linker approximately 7 nm long.<sup>68</sup>

#### 2.2.4 Linkers of With Programmable Elastic Compliance

To provide a flexible linker between the leucine zippers and the DNA scaffold, polypeptides based on the  $VPGV_\alpha G$  sequence of the natural polymer elastin were designed. Polypeptides built from these sequences have little secondary structure, and behave as nearly ideal elastomers with predictable spring constants (see table 2.1 for a list of physical constants).<sup>69</sup> This repetitive sequence is not labile to endogenous proteases, can be purified under denaturing conditions, and is stable under most labeling pHs. The elastin polymers exhibit a lower critical solution temperature (LCST) at elevated temperatures, in which the protein coacervates, expelling water trapped within the structure. This LCST can be tuned for elastin sequences by replacing the guest  $V_\alpha$  residue with varying amino acids.<sup>70</sup> This also can be used to alter features like the isoelectric point and solubility of these peptides by including charged and hydrophilic

residues. In previous work by Diehl *et al.*, the LCST property of phenylalanine substituted elastin peptides (ELF) was used to create switchable materials for microtubule gliding assays. In these experiments, the temperature could be used to modify the spring constant and length of the motor-surface linkages, effectively controlling the working distance of monomeric kinesin, and modulating the observed microtubule velocity.<sup>63</sup> For the present work, a serine substituted elastin sequence *ELS* (See (A) table 2.2) was used to create a hydrophilic polymer with an LCST well out of physiological range. The C-terminus of the elastin sequence included a single cysteine residue that allowed for the covalent modification of the polypeptide with a single strand of amine functionalized DNA, using the heterobifunctional linker, sulfosuccinimidyl 4-[N-maleimidomethyl]cyclohexane-1-carboxylate (sulfo-SMCC).<sup>71</sup>

Table 2.1 : Table of Mechanical Values for Elastin Polypeptides. Where the hydrodynamic radius is determined by  $d = \sqrt{mL_P}/\sqrt{6}$ , and the spring constant is calculated  $\kappa = 3k_B T/2L_C L_P$ .<sup>69</sup>

ELS Repeat	Residues	Hydrodynamic Radius $d$ (nm)	Persistence Length $L_P$ (nm)	Contour Length $L_C$ (nm)	Spring Constant $\kappa$ (pN/nm)
6	150	6.3	0.4	43.5	0.35
12	300	8.9	0.4	87	0.18
24	600	12.6	0.4	174	0.09

### 2.2.5 Tuning the System to Study Coupled Kinesin

The final structure produced by the self-assembling materials is composed of: (1) a motor protein fusion that includes the half of the coiled-coil pair forming leucine zippers ( $Z_E$ ), while the other half (2) of the zipper complex ( $Z_R$ ) is fused to the artificial protein linker that is labeled with a DNA strand addressing it to the overhangs of (3) the DNA scaffold. A scale diagram of the final assembly is shown in Figure 2.2. Standard recombinant techniques were used to generate a kinesin-1 fu-

sion construct,  $K560-eGFP-Z_E-(His)_6$ , that contained the first 560 amino acids of a N-terminal human kinesin, a green fluorescent reporter protein ( $GFP$ ), and the glutamic acid-rich zipper ( $Z_E$ ) which serves as a capture probe for the kinesin. The zipper is incorporated into the coiled-coil structure of the kinesin stalk, and should be a minimal disruption to its natural tertiary structure. The leucine zipper-based motor couplings are coiled-coil structures, reminiscent of the stalk of the full-length kinesin, and represent a minor perturbation to the system.

To make coupled complexes of kinesin motors, the long persistence length of DNA was utilized to build a scaffold separating the motors by 50 nm. At this spacing, effects from molecular crowding should be minimized, as coupled motors bound to the same protofilament the ability to take several 8 nm steps before steric effects become a significant factor. Below intermotor spacings of 30 nm, previous reports have shown that molecular crowding reduces the velocities of kinesin motors in microtubule gliding assays (*i.e.* at motor densities of  $< 1000$  molecules per  $\mu\text{m}^2$ , an effective linear density of  $\approx 32$  motors per  $\mu\text{m}$ ).<sup>72</sup> The incorporation of unpaired thymine bases into the overhangs adds some rotational flexibility to the final system. The synthetic DNA backbone grants the incorporation of modified bases which can impart experimental functionality, such as fluorescent dyes and biotin. As a further measure of control, the elastin-based scaffold linkages can be varied in length to modulate the degree of mechanical coupling of the motors. This provides a way to change the degree to which motors can impose forces on one another, and observe the impact of intermotor compliance on collective transport.

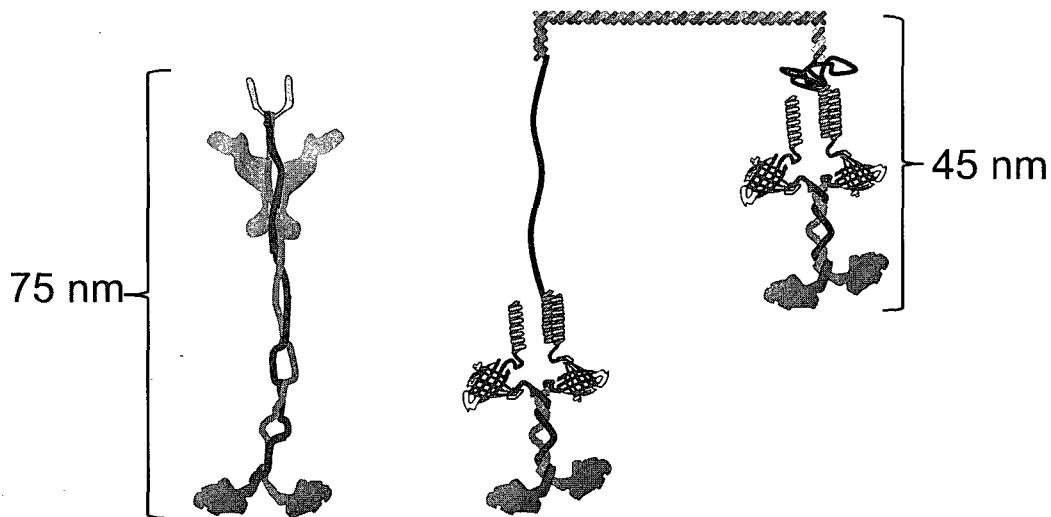


Figure 2.2 : A scale diagram of the coupled kinesin complex. A full-length kinesin is shown at left. The elastin domain (ELoS<sub>6</sub>) of the artificial protein linker is shown at full contour length (left scaffold attachment), and at its hydrodynamic radius of 6 nm (right scaffold attachment).

### 2.3 Verifying Formation of the Multi-Protein Assembly

Previously, binary protein complexes formed using this technique were isolated using non-denaturing PAGE,<sup>73</sup> showing formation with nearly quantitative yield ( $\approx 90\%$ ). While the DNA-artificial protein linker partial assembly was easily isolated using this method (see Figure 2.4), the size of the coupled kinesin complexes (180 kDa for each kinesin dimer) prohibited their direct characterization on PAGE. The formation of the complex was confirmed indirectly by experimental observations of 50 nm displacements in the trajectories created by fluorescently-labeled complexes (Figure 3.4, pp.57).

Further indirect evidence of the scaffold formation is shown in optical trapping assays that utilize the same coupled motor complexes. Here, the DNA scaffold is used set the distance between the two motors on a 500 nm polystyrene bead (See Figure



2.3 A). An infrared laser is then focused on the bead, which, because of the high refractive index of the material, bends the incoming beam, and imparts a force that ‘traps’ it at the beam center.<sup>74</sup> When the motor complex on the trapped bead binds to a surface-immobilized microtubule, it pulls the bead against the increasing load imparted by the beam until detachment occurs. The distances of the bead displacements can then be translated into force measurements. For coupled motor complexes, multiple traces contained clear signatures of collective motor function, both in the peak forces produced, and the microtubule unbinding dynamics of the assembly (Figure 2.3 C). Two-kinesin beads are capable of generating forces above 10 pN that are never produced in the single-kinesin version of the experiment. Instead, single-kinesin beads detach at or near the characteristic 7.6 pN stalling force for a single motor. Additionally, 43 % of the two-kinesin trajectories contained instantaneous rearward displacements to positions other than the trap center upon microtubule detachment. This behavior is clearly observed in the traces shown in Figure 2.3 C, and is indicative of a two-state unbinding process. This behavior is interpreted as the assembly partially detaching to a single-motor bound state and then completely detaching. If an assembly's leading or front motor detaches first, the bead will be displaced backwards until the remaining bound motor prevents further rearward motion by assuming the full load of the trap. Since the DNA scaffold specifies the distance between the motor-bead attachment sites, the magnitude of these rearward displacements should reflect the length of the DNA scaffold. This behavior is confirmed by the appearance of a 47 nm peak in a histogram of rearward displacement magnitudes (Figure 2.3 D), and verifies the presence of the complete kinesin assembly.

Microtubule gliding assays using a specific surface-anchoring technique that utilized the artificial protein linker gave further proof of the validity of the attachment

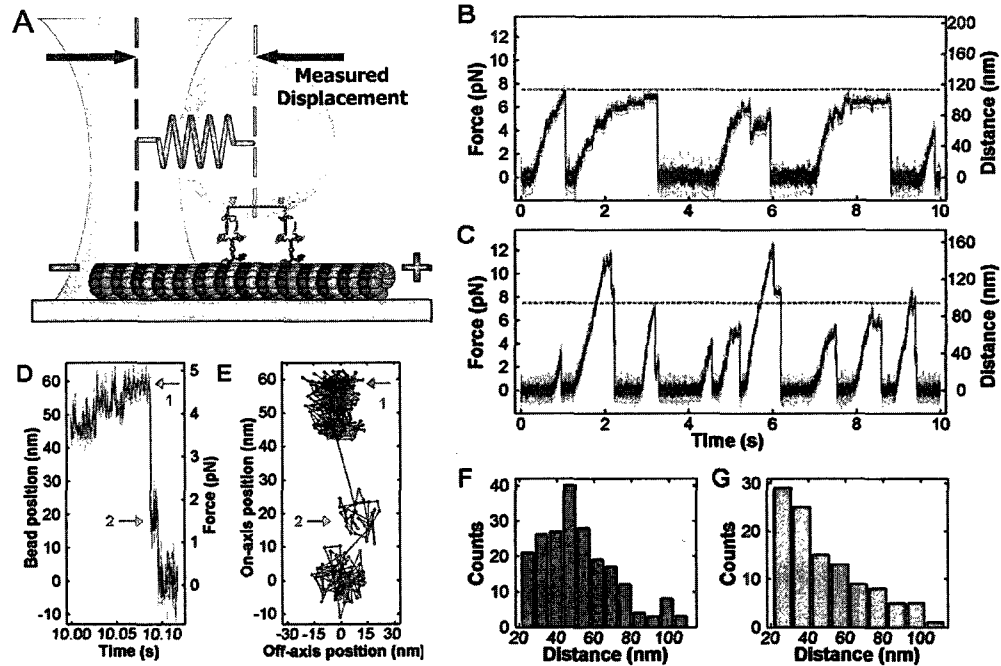


Figure 2.3 : Optical trapping of coupled motor complexes. (A) A diagram showing the coupled motor complex displacing a bead from the focus of the optical trap. As the bead is displaced, a force is imparted on the motors. (B) Single-motor displacements from trap center and force vs. time. The dashed line indicates the single motor stall force ( $\approx 7$  pN). (C) Coupled motor trapping data, showing enhanced force production ( $> 7$  pN). Also visible in the traces are single motor unbinding events that result in large instantaneous displacements of  $\approx 50$  nm. (D) Close-up of a single motor detachment event within a coupled motor trace. Here position 1 represents the initial two-motor complex position at high force prior to the detachment of the leading motor in the assembly, followed by a large displacement of 50 nm to position 2 before the entire complex detaches and returns to the trap's center. (E) The on- and off-axis movement of the same detachment event. (F) Histogram of rearward displacements for the coupled-motor complex. The pronounced peak at 50 nm reflects the length of the DNA scaffold that separates the two motors. (G) Histogram of single motor rearward displacements.

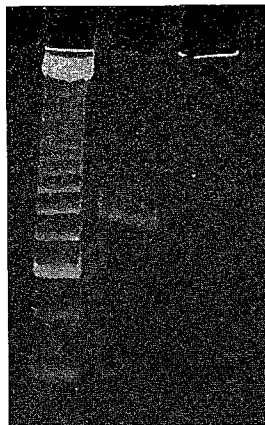


Figure 2.4 : A non-denaturing gel stained with ethidium bromide, showing the complexation of the 50 nm scaffold with the elastin based linking peptide/DNA conjugate. The first lane is a 25 bp standard (Invitrogen), the second is the 50 nm ruler ( $\approx 170$  bp), and the third is the partial assembly created by incubating the DNA scaffold and linker conjugate at a ratio of 1:2. Due to the strong charge of the linker conjugate, it remains in the well. The disappearance of the DNA band at 170 is taken to mean complete assembly.

chemistry. For the specific attachment of kinesin, a modified form of the gliding assay presented by Diehl *et al.*<sup>63</sup> was used, in which the DNA-conjugated protein linker was hybridized to a biotinylated DNA strand. This biotin linkage then mediated the attachment of single kinesin molecules to a streptavidin-coated surface generated on glass coverslips.<sup>75</sup> A detailed schematic of the specific attachment assay is shown in Figure 2.5. The average velocity for non-specifically bound *K560-eGFP-Z<sub>E</sub>-His* was  $309 \pm 151$  nm/s, while the specific attachment assay yielded an average velocity of  $408 \pm 200$  nm/s. Gliding assays performed on streptavidin surfaces in the absence of the biotinylated conjugate-linker exhibited no microtubule binding. Together, these results show that the conjugate-linker is effective as an anchoring chemistry, and shows that modulations in the length and compliance of the motor attachment can modify the microtubule gliding velocity. Similar studies have concluded that increasing the

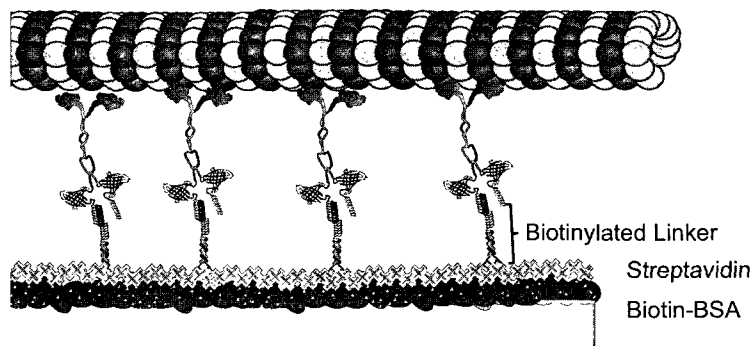


Figure 2.5 : Specific attachment of kinesin to a streptavidin surface. The surface was prepared by first attaching biotinylated-BSA to RCA-cleaned glass. Streptavidin was then used to link the kinesin to the surface *via* the biotinylated conjugate linker molecule.

length of the surface linkages increases observed velocities at high concentrations of motor by reducing the mutual interference between motors.<sup>49</sup> Chapter 3 shows further evidence of coupled motor complex formation in the trajectories of the coupled kinesin particles, Figure 3.5.

## 2.4 Chapter Conclusion

A strategy to couple two motor proteins together on a double-stranded DNA scaffold was created that employs self-assembling linker proteins covalently modified with single stranded DNA as an interface. This approach allows for the solution-phase capture of expressed fusion proteins, which can be purified under native conditions, while the capture probe can be purified and labeled under conditions that would otherwise damage the enzymatic activity of the motor protein. This system represents the first of its kind, where intermotor spacing is controlled using a rigid DNA spacer, and attachment stiffness is tuned by increasing or decreasing the number of

ELS repeats in the artificial linker protein. In addition, the DNA backbone can be modified to include various chemistries for surface-anchoring and fluorescent labeling. Attachment of proteins to the scaffold is mediated through single-strand overhangs that extend from the double-stranded backbone of the DNA. Here, the sequences can be chosen such that each attachment site is unique, and binate protein complexes can be synthesized. Therefore, this approach has broader utility in the study of any set of interacting proteins.

## **2.5 Methods for Building Self-Assembling Components**

### **2.5.1 Artificial Linker Protein Design and Purification**

Artificial proteins were used as a flexible linker between the rigid DNA backbone and the motor proteins. The construct chosen was composed of an arginine based leucine zipper,  $Z_R$ , six repeats of an elastin-based sequence, and a C-terminal cysteine that allows for maleimide modification of the protein. Genes encoding the artificial protein-based linker polymers began with a construct containing a single elastin repeat,  $ELS_1$ , and were polymerized further using recursive directional ligation.<sup>76</sup>

### **Generation of the Plasmids Encoding the Artificial Proteins**

Arbitrary DNA sequences can be generated using PCR by hybridizing overlapping oligonucleotides during the anneal step, and then allowing the polymerase to generate longer DNA fragments with each cycle until the target gene is produced. This target gene is then used as a template for amplification using a second PCR reaction with only the outermost primers. The online resource, DNAworks, was used to generate these overlapping oligonucleotide sequences to perform this reaction.<sup>77</sup> The protein

Table 2.2 : Sequences of artificial protein subunits. (A) The sequence for the elastin monomer,  $ELS_1$ , is shown with the repeating substitution of serine in the  $V_\alpha$  position. (B) The sequence of the leucine zippers  $Z_R$  and  $Z_E$  are distributed according to their heptad repeats. The alignment of the sequences at the  $g$  position highlights the charged arginine ( $R$ ) and glutamic acid ( $E$ ) residues that create strong electrostatic interactions that create a strong preference for heterodimeric assembly.

(A)							
$ELS_1$	[(VPGVG)(VPGSG)(VPGVG)(VPGSG)(VPGVG)] <sub>1</sub>						
(B)							
	<b>DEF</b>	<b>GABCDEF</b>	<b>GABCDEF</b>	<b>GABCDEF</b>	<b>GABCDEF</b>	<b>GABCDEF</b>	<b>GABCD</b>
$Z_R$	LEI	RAAALRR	RNTALRT	RVAELRQ	RVQRLRN	EVSQYET	RYGPL
$Z_E$	LEI	EAAALEQ	ENTALET	EVAELEQ	EVQRLEN	IVSQYRT	RFGPL

sequence for  $Z_R-ELS_1-C$  was entered, and a list of primers was generated that encoded the desired gene. The primers were then added stoichiometrically into a 10  $\mu$ M “master-mix” and 3  $\mu$ L was added to a standard PCR reaction, in place of the usual primers and template DNA. The thermal cycler programs for the two successive PCR reactions are shown in Table 2.3.

Table 2.3 : PCR protocol for DNAworks

Step	Oligonucleotide Assembly		Amplification	
	Temperature ( $^{\circ}$ C)	Time (seconds)	Temperature ( $^{\circ}$ C)	Time (seconds)
1 Melt	95	60	95	60
2 Melt	95	30	95	30
3 Anneal	50	30	$T_m-5$	30
4 Extension	73	50	73	50
5 Repeat	go to 2, 40 times		go to 2, 27 times	
6 Final Extension	72	480	72	480

After the first PCR reaction was completed, 1  $\mu$ L was added as template DNA to a fresh reaction mixture with the first and last primers, dNTPs, and polymerase. Following the PCR of the DNAworks primers, the final gene product was then purified using a PCR cleanup kit, digested with NcoI and HindIII, and ligated into the

pQE-60 (Qiagen) cloning vector between the same sites. The plasmid,  $Z_R\text{-ELS}_1\text{-C}$ , was then submitted for sequencing. Elastin multimers (*i.e.*  $\text{ELS}_{2-6}$ ) were generated using recursive ligation, as described by Schweller *et al.*<sup>73</sup>

### Purification and Labeling of Artificial Protein Linkers

The artificial linker,  $Z_R\text{-ELS}_6\text{-C}$ , was co-expressed with a secondary protein,  $Z_E\text{-(His)}_6$ . The secondary protein,  $Z_E\text{-(His)}_6$ , forms a stable coiled-coil complex with the  $Z_R\text{-ELS}_6\text{-C}$  protein, protecting it from proteolytic degradation, and providing a purification tag for isolation from lysates using Ni-NTA affinity.<sup>78</sup> The  $Z_R\text{-ELS}_6\text{-C}$  gene was built in a pQE series vector which confers ampicillin resistance, and the  $Z_E\text{-(His)}_6$  protein was ligated into the BglII site of pREP4, which confers kanamycin resistance. With this convention, colonies containing both plasmids could be selected by using media supplemented with both antibiotics.

Table 2.4 : Required reagents for denaturing purification

8 M Urea Lysis Buffer	100 mM	$\text{Na}_2\text{HPO}_4$
	10 mM	Tris·HCl
	8 M	Urea
	Adjust pH to 8.0	
8 M Urea Wash Buffer	100 mM	$\text{NaH}_2\text{PO}_4$
	10 mM	Tris·HCl
	20 mM	Imidazole
	8 M	Urea
	Adjust pH to 6.3	
6 M Guanidinium Chloride	100mM	$\text{NaH}_2\text{PO}_4$
	100 mM	Tris·HCl
	6 M	GuCl
	Adjust pH to 8.0	

The plasmids were co-transformed into BL21 cells and spread on agar plates that contained ampicillin and kanamycin. Colonies were isolated and grown to  $OD_{600} = 1$ , before adding 1 mM IPTG. The cultures were allowed to express for 16 hours at 37°C, before being transferred to 500 mL centrifuge tubes, and spun at 5,500 RPM for 15 minutes. The cell pellets were then collected, 5 mL of 8 M urea was added per gram of cells, along with a stir bar, and the mixture was transferred to a stir plate at 4°C overnight. The lysate was then moved to 50 mL tubes and clarified twice at 16,500 RPM for 30 minutes. The clarified lysate was then transferred to 50 mL disposable centrifuge tubes, incubated with Ni-NTA resin that was equilibrated with 8 M urea, and tumbled for 1 hour. The centrifuge tubes were then spun in a table-top centrifuge for 1 minute at 1,000 RPM to pellet the resin. After decanting the lysate, the resin was resuspended in 8 M urea supplemented with 20 mM imidazole, and transferred to a column. The wash was allowed to drain, and the  $Z_R-ELS_6-C$  protein was selectively eluted by dissociating the zipper complex with six 3 mL aliquots of 6 M guanidinium chloride (GuCl). The eluate was then passed through a second Ni-NTA column to eliminate any remaining  $Z_E-(His)_6$ . The fractions were then combined, placed in dialysis tubing with a 6-8000 kDa molecular weight cut off (18.4 kDa for  $Z_E-(His)_6$  MW), and dialyzed against millipore water for 2 days at 4°C, with 5 water changes a day. The resulting solution was transferred to a disposable 50 mL conical vial, frozen, and lyophilized to dryness.

In order to attach the artificial protein polymer to the DNA scaffold, it is necessary to conjugate a single strand of DNA to the protein that addresses it to the single-strand overhang of the DNA ruler. The C-terminal cysteine of the polymers was reduced and covalently linked to the amine terminated single-stranded DNA us-



ing the hetero-bifunctional crosslinking reagent SMCC.<sup>71</sup>

Table 2.5 : Required reagents for SMCC coupling

8 M Urea Buffer	100 mM	NaH <sub>2</sub> PO <sub>4</sub>
	10 mM	Tris·HCl
	8 M	Urea
	Adjust pH to 7.2	
10X PBS (1L)	14.4 g	Na <sub>2</sub> HPO <sub>4</sub>
	2.4 g	NaHPO <sub>4</sub>
	1.40 M	NaCl
	30 mM	KCl
	Adjust pH to 7.4	
Conjugation Buffer	20 mM	NaH <sub>2</sub> PO <sub>4</sub>
	80 mM	Na <sub>2</sub> HPO <sub>4</sub>
	150 mM	NaCl
	1 mM	EDTA
	Adjust pH to 7.3	
FPLC Buffer A	20 mM	Tris Base
	Adjust pH to 8.3	
FPLC Buffer B	20 mM	Tris Base
	1 M	NaCl
	Adjust pH to 8.3	

The lyophilized protein was solubilized at a concentration of 10 mg/ml in the 8M Urea, pH 7.2. The C-terminal cysteine was reduced by adding 450  $\mu$ L of the protein to 50  $\mu$ L of 400 mM TCEP (tris(2-carboxyethyl)phosphine), and the pH was adjusted to 4.5. The reaction was incubated for 1.5 hours at 37°C. While incubating, a Nap-5 column was equilibrated with 10 ml of 8 M Urea. After incubation, 500  $\mu$ L of the reduced protein was added to the Nap-5 column to remove excess reducing agent, and eluted with 1 ml 8M Urea pH 7.2, yielding a final volume of 1 ml. The amine DNA was then reacted with the NHS-ester of the sulfo-SMCC by combining 100  $\mu$ L

of amine-terminal DNA (100  $\mu$ M), 100  $\mu$ L conjugation buffer, and 60  $\mu$ L sulfo-SMCC (2 mg sulfo-SMCC/60  $\mu$ L DMF). This mixture was allowed to react at 37°C for 1 hour. A second Nap-5 column was equilibrated with 10 ml 1X PBS. After incubation, the DNA reaction was diluted by adding 240  $\mu$ L of conjugation buffer, and was then transferred to the Nap-5 column and eluted with 1 ml 1X PBS, yielding a final volume of 1 ml DNA. The DNA and reduced protein volumes were then added 1:1 in microcentrifuge tubes, wrapped in foil, and agitated with a shaker for 2 hours at room temperature. The shaker was then moved to a 4°C, and allowed to react overnight. The sample was then purified using FPLC with a Hi trap Q XL 5 mL column on a 1-100% NaCl gradient over 12 CV in 20 mM tris buffer (pH 8.3). The fractions, identified by UV absorbance (see Figures 2.6, and 2.7), were collected and analyzed using an SDS-PAGE gel treated with Stains-All to verify the presence of both DNA and protein in the sample. Fractions containing the DNA/protein conjugate were combined, lyophilized, redispersed in TAE+12.5 mM Mg(OAC)<sub>2</sub>, aliquoted, and then stored at -20°C.

### 2.5.2 DNA scaffold synthesis

The DNA scaffold was designed to provide a spacing of 50 nm between neighboring motors, and to allow for the inclusion of single, or multiple biotin insertions within the backbone. Scaffolds were created from two single strands, each consisting of 170 nucleotides. Once annealed, these strands form a duplex containing 148 paired bases (14 helical turns) and flanked by single-stranded, 20 base overhangs on each end (see Figure 2.8, shown with two biotins). The nucleotide sequence of the overhang

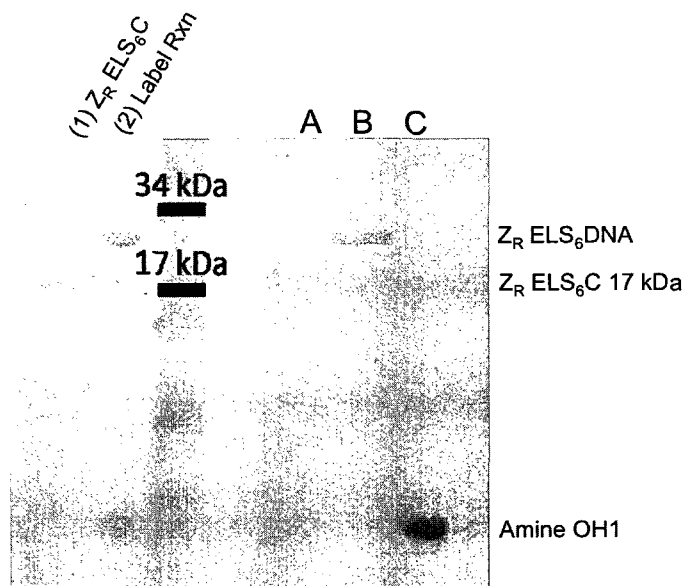


Figure 2.6 : Denaturing PAGE gel of FPLC fractions from the DNA conjugation reaction (reproduced from Schweller *et al.*).<sup>73</sup> Gel is developed using Stains-All, which stains protein yellow (faint light gray), and DNA blue (dark gray). (1) Unlabeled  $Z_R ELS_6 C$ , (2) DNA conjugation reaction mixture; and FPLC fractions: (A) free protein, (B) artificial protein/DNA conjugate, and (C) unlabeled DNA.

region was designed to be complementary to the 20 nucleotides conjugated to the artificial protein linkers. The ssDNA overhangs also contain two thymine bases that remain unhybridized in the full assembly to provide flexibility between the overhang sequence and the DNA backbone. The software program SEQUIN was used to assign the nucleotide sequence of the scaffolds to minimize unwanted secondary structures and undesired interactions between the strands.<sup>66</sup> A table of the physical constants for the generated strands is shown in table 2.10. The final 170 base DNA strands were each created from 4 separate ssDNA oligomers (see table 2.11) that were individually PAGE-purified, and then ligated together using a splint ligation procedure. During

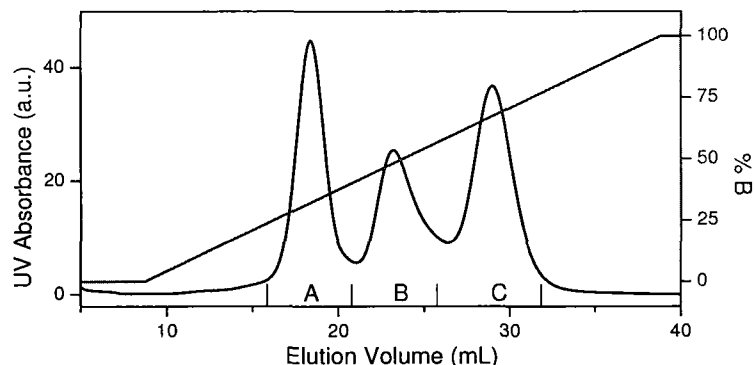


Figure 2.7 : DNA-conjugated polymers were purified to homogeneity using fast protein liquid chromatography (FPLC) and a HiTrap QXL ion exchange column with a gradient of 0–1 M NaCl over 12 column volumes. Three peaks were isolated corresponding to (A) free protein, (B) artificial protein/DNA conjugate, and (C) unlabeled DNA.

this step, a single biotin-functionalized oligomer was introduced. When incorporated into the scaffold, the biotin molecule is positioned asymmetrically on one end of the duplex, and is inserted one half turn away from the junction between duplex region and the ssDNA overhang. After their synthesis, the two full-length ssDNA strands were purified and then annealed together to form the complete scaffold. Duplex formation and the absence of excess ssDNA were confirmed using non-denaturing PAGE analysis.

### Parent Strand Assembly

Before further modification of DNA strands, incomplete products from synthesis are removed using polyacrylamide gel electrophoresis under denaturing conditions (8 M urea). The smaller strands ( $\leq 30$ ) are run on a 20%, intermediate strands (30 to 50) on a 15% gel, while longer strands ( $>50$ ) are run on 10% gels.

Table 2.6 : Required Buffers for Denaturing Purification of DNA Strands

10X Tris Borate EDTA	890 mM	Tris
	890 mM	Boric acid
	20 mM	EDTA
20% Acrylamide in 8 M Urea (500 mL)	250 mL	40% Acrylamide 19:1 bis:tris
	250 g	Urea
	50 mL	10X TBE
8 M Urea in TBE (500 mL)	250 g	Urea
	50 mL	10X TBE
Extraction Buffer	500 mM	Ammonium acetate
	11 mM	Magnesium acetate
	1 mM	EDTA

For example, to prepare a 15% acrylamide gel in a 16X16 cm caster with 1.5 mm spacers, a total volume of 40 mL of acrylamide solution is made.

Table 2.7 : Denaturing Acrylamide Gel Protocol

## Denaturing Acrylamide Gel (40 mL)

10 mL	8 M Urea in TBE
30 mL	20% acrylamide
400 $\mu$ L	10% APS
20 $\mu$ L	TEMED

The solution is poured into the caster, removing all air bubbles from the gel, and allowed to polymerize for 10 minutes. The strands are loaded into the wells at a concentration of 100  $\mu$ M with 50 % volume denaturing dye (90 % formamide, 10 mM NaOH, and bromophenol blue). In a gel runner heated to 45°C the gel was run at 500 V with 1X TBE. The time needed was dependent on the size of the product to be purified. Gels were removed from the apparatus and stained in a solution of ethidium bromide. Bands of the appropriate length were removed under UV illumination. The

gel pieces are submerged in 500  $\mu\text{L}$  extraction buffer and allowed to shake at  $4^\circ\text{C}$  for 2 days.

### **Extraction of DNA from Gels**

The gel pieces were pelleted with a quick spin in the microcentrifuge and the extraction buffer was removed. The gel bits were washed with 200  $\mu\text{L}$  of nuclease-free water, and the fractions were combined in a microcentrifuge tube. 700  $\mu\text{L}$  of butanol was added to the extract and mixed thoroughly. The butanol layer was allowed to separate, and the organic phase (top) was removed. Butanol washing was repeated until the aqueous volume was  $\approx 100$   $\mu\text{L}$ . Then, 1.2 mL of ethanol was added, and the reaction was placed at  $-80^\circ\text{C}$  for 45 minutes. The tubes were at max speed for 30 minutes to pellet the DNA. Next, 1 mL of cold 70% ethanol (stored at  $-20^\circ\text{C}$ ) was added carefully, to avoid disturbing the pellet, and the tube was centrifuged at max for 10 minutes. The supernate was then poured off, and the remaining solvent was dried under vacuum. The DNA product was then dissolved in a small volume ( $\approx 30$   $\mu\text{L}$ ) of TAE with 12.5 mM  $\text{Mg}(\text{OAc})_2$ , and frozen until used.

### **Building the Strands Using Splint Ligation**

The smaller constituent strands were ligated together using a splint ligation procedure, in which a sacrificial strand (one that does not participate in the reaction) is hybridized to the reactant strands to hold the ends to be ligated in close proximity. Before ligation, the 5' end of synthetic DNA strands were phosphorylated in preparation for the ligase reaction. The total ligation procedure has an estimated yield of 300

pmol, so 50  $\mu\text{L}$  of single stranded DNA at a concentration of 70  $\mu\text{M}$  were prepared for the phosphorylation reaction were prepared.

Table 2.8 : Protocol for Phosphorylation Reaction

Phosphorylation Reaction (20 $\mu\text{L}$ )	
14 $\mu\text{L}$	Purified DNA strand
2 $\mu\text{L}$	10 mM ATP [1mM]
2 $\mu\text{L}$	10X ligase buffer
2 $\mu\text{L}$	T4 polynucleotide kinase

A pipette was used to mix the reaction thoroughly before placement in a 37°C incubator for one hour. The strand concentrations after phosphorylation were assumed to be 50  $\mu\text{M}$ .

The strands to be ligated were then added together at a target concentration of 300 pmol and annealed before the addition of buffer and ligase. The anneal reaction was used to completely dissociate the double-stranded DNA at high temperatures, and using a step-down temperature gradient, cooled slowly to allow for proper base-pair hybridization and minimization of secondary structure. The thermal cycler program is shown below.

Ligase was then added to the reaction and allowed to react for 16 hours (overnight). The mixture was then purified using denaturing gel electrophoresis as described above.

The exact synthesis route for the 50 nm ruler with two biotin strands is as follows. Anneal Sac1, phosphorylated DHR-5 bio, and DHR-11 at 1:1:1 concentrations, then ligate overnight. In a separate reaction vessel, anneal and ligate Sac 3, phosphorylated strands DHR-2 bio, and DHR-9. A denaturing purification with a 15% denaturing gel is performed and the product bands are isolated and extracted for 2 days at 4°C.

Table 2.9 : Thermal Cycler Protocol for DNA Annealing Reaction

Anneal Thermal Cycle	
Temp (°C)	Time (min)
95	3
90	3
90→75	10
75→60	15
60	10
60→45	10
40	5
30	20
25	20

Each ligated strand is then isolated with butanol precipitation, dried, and solubilized in TAE with 12.5 mM Mg(OAc)<sub>2</sub>. The product strands, DHR-9+2 bio and DHR 11+5 bio, are combined with DHR-8 and DHR-10, annealed, and ligated overnight. Denaturing purification and butanol extraction is used to isolate the strands. The final stands are combined along with DHR-1 and DHR-3 annealed, and used as described in chapter 3.

### 2.5.3 Creation of Kinesin Fusion Plasmids and Motor Expression

All plasmids were amplified in Stratagene's XL1-Blue and sequenced to verify fidelity of the construct. Standard recombinant techniques were used to generate a kinesin-1 fusion construct, *K560-eGFP-Z<sub>E</sub>-(His)<sub>6</sub>*, that contained the first 560 amino acids of a N-terminal human kinesin, a green fluorescent reporter protein (*GFP*), and a heterodimerizing glutamic acid rich zipper (*Z<sub>E</sub>*) which would serve as a capture probe for the kinesin. The cloning scheme utilized the *K560-GFP-(His)<sub>6</sub>*<sup>27,28</sup> plasmid (a



Table 2.10 : Physical Constants of the Strand Segments that make up the 50 nm Ruler

Strand Name	Bases	Mol. Wt. (kDa)	$\epsilon$ for $A_{260}$ ( $M^{-1}cm^{-1}$ )
DHR 1	16	5	153,900
DHR 2	38	11.7	362,900
DHR 2 bio	37	12.1	362,900
DHR 3	10	3	89,300
DHR 5	32	9.8	303,900
DHR 5 bio	31	10.2	303,900
DHR 8	58	18	555,000
DHR 9	58	18	566,000
DHR 10	70	21.4	650,800
DHR 11	58	17.7	541,100
Sac 1	45	13.9	426,000
Sac 3	45	13.8	410,000
AmineOH1	20	6.2	185,500

Table 2.11 : Sequences of the oligonucleotides that were used to make the 50 nm DNA rulers

Strand	Sequence (5' to 3')
DHR-1	GTCACGGACTGAGCGT
DHR-2	CGTAGCAGGCACATCGTTGGCTGGATAGACCGCATTTCG
DHR-2-Bio	CGTAGCAGGCACA/iBiodT/CGTTGGCTGGATAGACCGCATTTCG
DHR-2 Blunt	CGTAGCAGGCACATCG
DHR-3	CGATGTGCCT
DHR-5	AGTCCGTGACTTGGCTGGATAGACCGCATTTCG
DHR-5 Bio	AGTCCG/iBiodT/GACTTGGCTGGATAGACCGCATTTCG
DHR-8	CGTATGGTAAGCGGCTCGCAATCAGCTCTGACGAGTCTGTAG GTGTCGGATGCCGAAC
DHR-9	CTGAATAGGCGATAACCGATTAGTGGACGTGGCGTGCGTAATG AGTTCACTGGCAGCAC
DHR-10	GCTACGGTGCTGCCAGTGAATCATTACGCACGCCACGTCC ACTAATCGGTATCGCCTATTCAGGTTTCGG
DHR-11	CATCCGACACCTACAGACTCGTCAGAGCTGATTGCGAGCCG CTTACCATAACGACGCTC
Sac-1	GTCACGGACTGAGCGTCGTATGGTAAGCGGCTCGCAATCAG CTCT
Sac-3	CGATGTGCCTGCTACGGTGCTGCCAGTGAATCATTACGCA CGCC
Amine OH1	/5AmMC6/CGAATGCGGTCTATCCAGCC



generous gift from the Ron Vale lab at UCSD). A precursor plasmid was generated that contained *GFP-Ze-(His)<sub>6</sub>* and inserted between the KpnI and XhoI sites in Ron Vale's construct, effectively removing the existing GFP and histidine purification tag, replacing it with the desired sequence. The full length construct is 97.1 kDa, and 194.2 kDa as a dimer.

## **Expression and Native Purification of Kinesin**

### **Expression of Kinesin Constructs in *E. coli***

Beginning with a BL21 cell stock that was transformed with the plasmid, a plate was streaked and grown overnight at 37°C. The following morning, colonies were picked and grown to saturation in 5 mL 2xYT supplemented with corresponding antibiotics. Two liters of TB media were inoculated and grown until  $OD_{600} = 1$  at 37°C. IPTG was added to 1 mM to induce protein expression. After 12-16 hours for expression cells were pelleted at 5,500 RPM for 15 minutes at 4°C. 40 mL of lysis buffer (pH 7.6) per 1 L was prepared with an added protease cocktail: 1 mg/mL lysozyme, 1 µg/mL leupeptin and pepstatin, 1 µg/mL aprotinin, 1 µg/mL chymostatin, 1 mM pefabloc, 5 mM TAME, 5 mM PMSF, 1 mM ATP, and 1 mM βME. Cell pellets were collected and resuspended in lysis buffer, supplemented with 1mg/mL lysozyme, and protease inhibitor cocktail. A stir bar was added, and the tube was allowed to incubate for 30 minutes at 4°C on a stir plate. The solution was then snap-frozen and chopped finely when sufficiently thawed. Another aliquot of lysis buffer supplemented with protease inhibitors, βME, ATP, and 8 mg of DNase, was then added to the pellet. The lysate was then clarified by centrifugation at 16.5k rpm in 50 mL centrifuge tubes for 15 minutes. The supernate was transferred to fresh tubes, and spun again for 30

Table 2.12 : Required Buffers for Expression

TB Broth (1L)	16 g	Casein
	24 g	Yeast Extract
	4 mL	Glycerol
	900 mL	H <sub>2</sub> O
	Autoclave, add 100mL10X TB Salt	
10X TB Salts	2.31 g	Monobasic KHPO <sub>4</sub>
	12.54 g	Dibasic K <sub>2</sub> PO <sub>4</sub>
	100 mL	H <sub>2</sub> O
2xYT Growth Media and Plates	16 g	Casein
	10 g	Yeast Extract
	5 g	NaCl
	‡ For Plates, Add 15 g/L Agar Autoclave	
Lysis Buffer	50 mM	HEPES pH 6.8
	2 mM	MgCl <sub>2</sub>
	1 mM	EGTA
	50 mM	NaCl
	5%	Sucrose
	10 $\mu$ M	ATP
FPLC Buffer A	50 mM	HEPES pH 6.8
	2 mM	MgCl <sub>2</sub>
	1 mM	EGTA
	5%	Sucrose
	10 $\mu$ M	ATP
FPLC Buffer B	50 mM	HEPES pH 6.8
	2 mM	MgCl <sub>2</sub>
	1 mM	EGTA
	1 M	NaCl
	5%	Sucrose
	10 $\mu$ M	ATP

minutes. The Ni-NTA resin was then equilibrated with lysis buffer; 2-4 mL of resin per 50 mL lysate. The lysate was added to the resin and incubated at 4°C for 1 hour. The resin was pelleted at 1,000 RPM for 2 minutes and the supernate was discarded. Next, the resin was washed with 20 mM imidazole lysis buffer supplemented with ATP and  $\beta$ ME, then transferred to a protein purification column. The protein was eluted with 6 X 700  $\mu$ L aliquots of 400 mM imidazole lysis buffer supplemented with ATP. Here, elutions were either snap-frozen and stored at 80 °C, or further purified using FPLC.

For FPLC purification, the most concentrated fractions were combined and diluted 10-fold into buffer A. A MonoQ 1 mL column was equilibrated with 5% FPLC buffer B, and the motor fractions were loaded in 5 mL injections. A 5-100% gradient was then performed over 8 column volumes. The protein eluted at 30% B,  $\approx$  300 mM NaCl (see Figure 2.10), fractions were collected, snap-frozen, and stored at -80°C.

Before use, protein motors were purified using microtubule affinity to select for active motor, while removing impurities and C-terminal truncations (See Figure 2.9).<sup>79</sup> Frozen motor aliquots were thawed and transferred to dialysis tubing with a MWCO < 80 kDa, and dialyzed into BRB80 for 30 minutes. Microtubules were either purified from bovine brain,<sup>80,81</sup> or purchased from Cytoskeleton. For each 400  $\mu$ L aliquot of motor protein, 250  $\mu$ g of tubulin was placed into a 37°C incubator, along with the TLA 100.1 rotor, and allowed to polymerize for 10 minutes. After the microtubule polymerization step, taxol was added to 10  $\mu$ M. The full-length microtubules were then pelleted through 300 $\mu$ L of taxol cushion buffer, washed with BRB80, and resuspended in BRB80 containing taxol. The microtubules were then combined with the

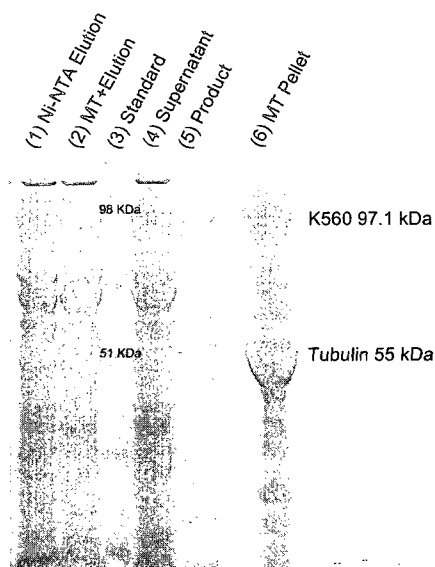


Figure 2.9 : PAGE gel showing the affinity purification of *K560-eGFP-Z<sub>E</sub>-His*. (1) Ni-NTA purified kinesin elution, (2) incubation of elution with polymerized microtubules, (3) protein standard, (4) supernatant after kinesin saturated microtubules have been pelleted through the glycerol cushion, (5) active purified kinesin, and (6) remaining microtubule pellet.

motor fraction, along with 5 mM AMP-PNP, and taxol. The mixture was incubated at room temperature for 15 minutes, and pelleted through the 600  $\mu$ L of cushion buffer as before. The pellet was washed, and resuspended in BRB80 supplemented with 400 mM KCl, taxol, 10 mM ATP. The mixture was allowed to incubate for 5 minutes, transferred to a new tube, and pelleted at 80 kRPM for 5 minutes. The motor-containing supernate was aliquoted and snap-frozen until use. Kinesin concentrations were determined by PAGE gel analysis by comparison with an unstained protein standard.

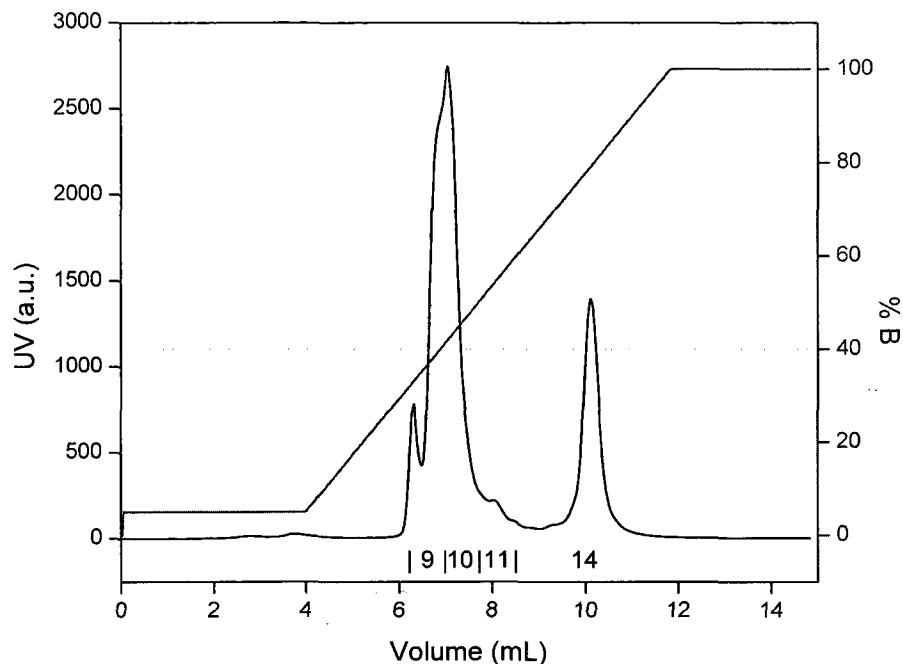


Figure 2.10 : FPLC chromatogram of the kinesin purification. Fraction 10 contained the active motor fraction

### Verification of Component Self-Assembly

Partial assemblies of the 50 nm DNA scaffold and the artificial protein linkers are created by incubating the two at a ratio of 1:2 DNA scaffold/Linker, and incubating at 4°C overnight. The partial assembly is isolated using non-denaturing PAGE, as shown in Figure 2.4. The procedure for non-denaturing PAGE on a 10 cm X 10 cm gel is as shown in Table 2.13:

The gel is then run at a voltage setting of 120 volts for 3-4 hours. Staining is then done using ethidium bromide to test for the presence of DNA, or alternatively, stained with stains-all to detect protein (yellow) as well as DNA (blue). Previously, complexes of two proteins have been isolated on non-denaturing gels as presented by Schweller *et al.*,<sup>73</sup>. Attempts to isolate the dual-kinesin complex on a non-denaturing

Table 2.13 : Protocol for Non-Denaturing PAGE

## Non-denaturing Polyacrylamide Gel (10 mL)

Non-denaturing gel	
1.75 mL	19:1 bis/tris 40% acrylamide
8 mL	TAE + 12.5 mM MgSO <sub>4</sub>
200 $\mu$ L	10% APS
10 $\mu$ L	TEMED
Modified TAE	
40 mM	tris base
40 mM	acetic acid
100 $\mu$ M	EDTA
	pH 8.0

gel were not successful, due largely to the prohibitive size of the entire complex. With each kinesin dimer at  $\approx$ 190 kDa, the DNA/protein assembly never entered the gel, regardless of gel percentage. Alternative methods of characterization were used during assays of single kinesin complexes, as presented in Chapter 3.

### Assessment of Motor Construct Activity and Specificity of Zipper Attachment

Further verification of the coiled-coil complex formation between the motor construct and the artificial linker was accomplished through specific surface attachment in a modified gliding assay. To anchor the kinesin to coverslips, a modified form of the gliding assay presented by Diehl *et al.*<sup>63</sup> was used, in which a DNA conjugated linker protein hybridized to a biotinylated DNA strand mediated the attachment of single kinesin molecules to a streptavidin coating.<sup>75</sup> A detailed schematic of the specific attachment assay is shown in Figure 2.5. The measurement of velocities of gliding microtubules was determined by the Gaussian fitting of histograms of instantaneous ve-



locities generated by the freeware RETRAC. The average velocity for non-specifically bound *K560-eGFP-Z<sub>E</sub>-His* was  $309 \pm 151$  nm/s, while the specific attachment attachment assay yielded an average velocity of  $408 \pm 200$  nm/s. Gliding assays performed on streptavidin surfaces in the absence of the biotinylated conjugate-linker exhibited no microtubule binding. This dual result shows that the conjugate-linker is effective as an anchoring chemistry, and shows that modulating the length and compliance of the motor attachment can modify the microtubule gliding velocity.

Table 2.14 : Required Reagents for Gliding Assays

BRB80	80mM	PIPES	
	2 mM	MgSO <sub>4</sub>	
	1 mM	EGTA	
BRB80 Cushion	80mM	PIPES	
	2 mM	MgSO <sub>4</sub>	
	1 mM	EGTA	
	8 M	Glycerol	
10X Gloxy	30 mg	Glucose Oxidase (150 mg/mL)	
	60 $\mu$ L	Catalase (20 mg/mL)	
	200 $\mu$ L	BRB80	
		Pass through 0.2 $\mu$ m filter 2X	
		Store at 4°C	
		1 M	Glucose
		143 mM	$\beta$ ME
		200 mM	ATP
		1 mM	100X Taxol

In preparation for the gliding assay, fluorescent tubulin was reconstituted at a ratio of 1:4 labeled to unlabeled tubulin. After polymerization at 37°C for 10 minutes, 5  $\mu$ g of microtubules were suspended in 50  $\mu$ L BRB80 supplemented with 1 mM taxol. The microtubules were then pelleted at 17,000 RPM for 25 minutes at room temperature, and resuspended in another 50  $\mu$ L BRB80 supplemented with 1

mM taxol. The working stock of microtubules was created by diluting this mixture tenfold.

For a non-specific attachment assay, motor stocks were perfused into a flow chamber at high concentrations, usually directly from Ni-NTA, FPLC, or microtubule-affinity elution. The motors were then allowed to incubate for 10 minutes on the bare glass surface of the perfusion chamber, and then a wash was performed with a chamber volume of 1 mg/mL  $\alpha$ -casein solubilized in BRB80. Following the casein wash, fluorescent microtubules were introduced into the chamber in an imaging solution comprised of BRB80, an oxygen scavenging system, taxol and ATP. The flow chamber was then sealed with nail enamel and visualized using TIRF microscopy.

Specific attachment of kinesin to a streptavidin surface was mediated by using the DNA conjugated  $Z_R$ - $ELS_6$  construct hybridized to a strand of DNA that was covalently modified with a single biotin. Flow chambers were assembled using RCA (1:1:5,  $\text{NH}_4\text{OH} : \text{H}_2\text{O}_2 : \text{H}_2\text{O}$ ) cleaned slides and coverslips, with two strips of double-sided tape to create a channel. A single chamber volume of 1 mg/mL biotinylated-BSA was then deposited for 10 minutes, followed by a wash of 1 mg/mL  $\alpha$ -casein in BRB80. A solution of 1 mg/mL streptavidin was then perfused into the chamber and incubated for 10 minutes before a second wash with casein. During this initial slide prep the motor was combined with DNA conjugate (that was hybridized 1:1 with the biotinylated DNA overnight) at a ratio of 4:1 motor to conjugate and allowed to associate for 30 minutes. The biotinylated motor construct was then added to the streptavidin treated slide and allowed to settle for 7 minutes. The excess motor was washed out with casein, and the microtubules were introduced to the chamber,

and incubated for 5 minutes. The chamber was then exchanged with imaging buffer; BRB80 with 2 mM ATP, 1X Gloxy, 40 mM glucose, 1.43 mM  $\beta$ ME and 10  $\mu$ M taxol. After sealing with nail enamel, the chamber was then imaged using TIRF microscopy.

## Chapter 3

# Negative Interference in Coupled Kinesin at Zero Load

### Chapter Outline

Kinesin-1 is a microtubule-dependent protein that uses the hydrolysis of ATP to generate piconewton-scale forces to haul cargos within the cell. Although many single molecule experiments have characterized the motor in isolation, the collective mechanics of motor groupings are not well understood, and characterized by experiments with no ability to detect or control the number of motors engaged during measurement. Here, a convergent synthesis approach uses the self-assembly properties of DNA and coiled-coil forming peptides to form well-defined complexes of exactly two kinesin. A single biotin labeled base in the DNA backbone of the assembly was labeled with a streptavidin-coated quantum dot (QD), that allowed the transport properties of the assemblies to be determined using total internal reflectance fluorescence microscopy (TIRF). The results from these experiments show that the average coupled motor run length is slightly longer than for the single motor, but not as long as predicted by an existing transition state model. Furthermore, at limiting ATP concentrations, single motor complexes exhibited clear 8 nm stepping, while the presence of fractional stepping and large instantaneous displacements were observed in the two motor case. These results, when combined with the observations of enhanced partial detachment and protofilament switching behavior, lead to the hypothesis that strain in the inter-

motor linkages created by asynchronous stepping increases the rate of transition to a single motor bound transport state. Much of this work was published in the 2009 paper “Negative interference dominates collective transport of kinesin motors in the absence of load”, published in the journal, *Physical Chemistry Chemical Physics*.<sup>82</sup>

### 3.0.4 Preconceptions of Grouped Kinesin Behavior

In cells, cargos that rely on kinesin-dependent transport exhibit behavior (*e.g.*, longer run lengths, increased maximum velocities, and higher force production) that is believed to be the work of multiple motors. It is generally assumed that the more motors available on a cargo, the longer the possible run length, due to the doubling of the binding capacity.<sup>30</sup> The presence of high concentrations of motors adhered to beads also show increases in the maximal force output, due to the engagement of multiple motors in transport.<sup>31</sup> Though some of the natural cellular behaviors have been recapitulated in non-specific arrangements of motors anchored to solid supports, the fundamental structural and mechanical principles that lead to collective behaviors are not well understood. In a collective kinesin assay on unilamellar vesicles, super-stall forces (27 pN) must be generated by groups of kinesin to extract membrane tubules. If the single-stall for a single kinesin is 7 pN, one would expect that 4 coordinated kinesin motors would be needed. Through experimental interpretations with theoretical modeling, it is determined that teams of 6-9 are needed to generate sufficient force due to the inefficiency of the enzyme’s asynchronous stepping.<sup>50</sup> Modified microtubule gliding assays in which motor position and stepping are measured also show the presence of asynchronous behavior, through the presence of fractional step sizes at low ATP<sup>46</sup> that are the result of linkages between uncoordinated motors stretching and compressing, causing a system relaxation that absorbs a fraction of the 8 nm ad-

vancement. Together, these observations indicate that the collective motor stepping is not synchronized, and the consequences are directly reflected in the mechanics of the motor's attachment to its nearest neighbor.

In the vesicle pulling experiment, motors must cluster at the pulled tips to aid in transport. Due to the fluid-like surface of the membrane, motors cannot apply tangential forces, only additive normal forces. Here, the nature of the motor attachment is different than the elastic, surface-mounted attachments presented in the bead assays. Together, these observations of enhanced transport by multiple kinesin molecules clearly illustrate that the kinetics of microtubule binding and unbinding, the mechanical properties of transported cargos, and the elasticity of individual motor linkages are all important factors that define the collective properties of interacting systems of motors. Assays that permit evaluation of cargo velocities and run lengths produced by precisely-defined motor assemblies must be developed to gain further insight into how structural features affect the observed transport phenomena.

### **3.0.5 Building Coupled Kinesin Complexes**

In Chapter 2 (pp. 14) of this work, a convergent self-assembly method was introduced to arrange kinesin proteins on a linear scaffold, with defined geometric spacing and elastic linkages. Coupled motor assemblies were composed of a single duplex of DNA that was used as a molecular scaffold, created from two single strands, each consisting of 170 nucleotides. Once annealed the strands formed a duplex containing 148 paired bases (14 helical turns) flanked by single-stranded 20 base pair overhangs on each end. Kinesin motors are anchored to the DNA scaffold through DNA-conjugated protein polymers that allow motor proteins to be captured in solution through the coiled-coil associations of an engineered parallel pair of heterodimeric leucine zippers<sup>67</sup> and

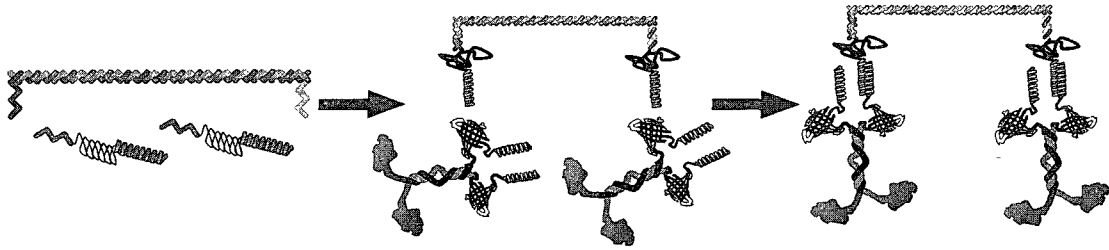


Figure 3.1 : Assembly of coupled-kinesin motor scaffold. The DNA ruler overhangs are complexed with the the conjugate linkers creating partial-assemblies. The kinesin is then added in excess to drive assembly of the final structure and minimize crosslinking.

attached to the scaffold *via* DNA-hybridization.

The coupled motor complexes were made by forming ‘partial assemblies’ by mixing the scaffold and artificial linkers, and then adding the motor in excess to drive the formation of the complete assembly and minimize crosslinking (see Figure 3.1). In the final assembly the DNA scaffold provides an intermotor spacing of 50 nm between neighboring motors (sufficient to avoid steric effects)<sup>72</sup>, and the spring constant of the elastic linkers  $\kappa$  was reported to be  $\approx 0.2$  pN nm<sup>-1</sup> when coupled with the kinesin stalk. For imaging the complexes, a single QD was placed asymmetrically on the coupled motor complex proximal to one of the motors (see Figure 3.2, panel B).

### 3.0.6 Kinesin Motility on Surface-mounted Axonemes

Initial experiments on fluorescent microtubules resulted in sparse fields of microtubules with vanishingly small numbers of single molecule encounters. Increasing the microtubule concentration enhanced the formation of antiparallel groupings of microtubules that resulted in the bidirectional transport of QDs coated with coupled motor complexes. To circumvent these problems sea urchin axonemes were prepared using

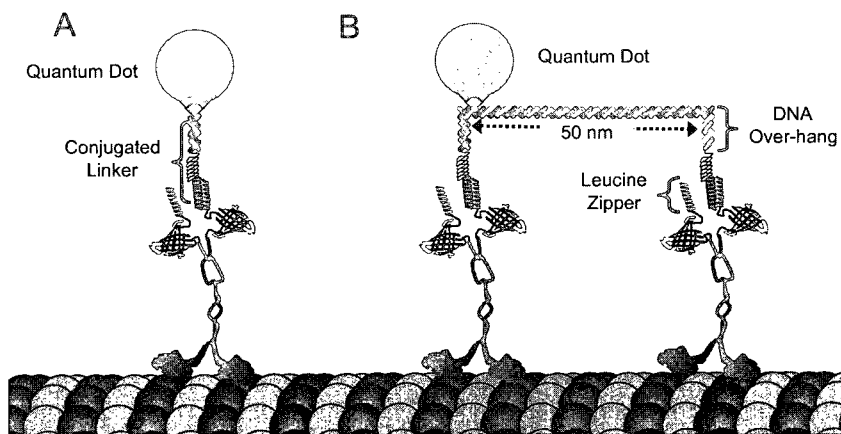


Figure 3.2 : Single molecule assay format. (A) The single motor is attached to the QD through a coiled-coil association of the leucine zipper domain of the biotinylated conjugated linker. (B) Coupled motors are built on a 50 nm scaffold of DNA, here the conjugate linkers hybridize to single strand overhangs extending from the double stranded backbone. A single biotin asymmetrically labels the scaffold, which was used as an indication of the binding state of the proximal motor.

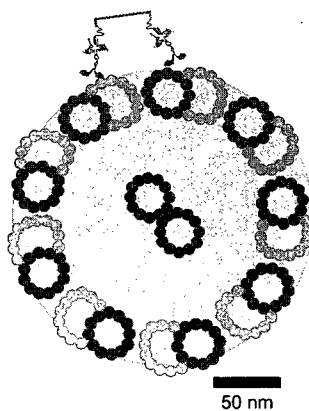


Figure 3.3 : Diagram of axoneme structure showing 9+2 arrangement of the doublet microtubules around the single center pair. The darker microtubules consist of 13 protofilaments, while the lighter colored doublets contain an added 10 protofilaments. A representation of the dual kinesin assembly is shown to scale.



a modified procedure developed by Gibbons and Fronk.<sup>83</sup> Axonemes possess a 9+2 arrangement of doublet microtubules around a central pair of single microtubules (see Figure 3.3).<sup>84</sup> The axonemal microtubules provide a series of long polarized tracks that can be easily reproduced, unlike inconsistencies encountered with the microtubules.

### 3.0.7 Signatures of Coupled Motor Transport

A single biotin molecule incorporated into the backbone of the DNA scaffold allowed motor assemblies to be functionalized with a streptavidin-coated QD, facilitating the tracking of individual motor assemblies, and the recording of trajectories. Representative trajectories for two-motor assemblies moving on axonemes and in the presence of 2 mM ATP are shown in (Figure 3.4). The coupled motor trajectories also gave distinctive signatures not present during in the single motor traces. Many traces possessed large and near-instantaneous motions of the QD that occur with a higher frequency than those previously reported,<sup>50,51,85</sup> While these motions occurred both on and off the main axis of the axoneme, the magnitudes of these displacements were commonly near commensurate with the 50 nm length of the DNA scaffold (see Figure 3.5). This behavior is interpreted as a single motor within a system unbinding, diffusing, and rebinding to the same or neighboring constituent microtubules of the axoneme. Considering the asymmetric positioning of the QD along the DNA scaffold, the large displacements of the two-motor assemblies most likely arise from the unbinding of the motor proximal to the QD and the subsequent rotation of the motor assembly about the remaining attached motor. Average velocities were determined by measuring the slope of the on-axis trajectory across entire run lengths.

QD velocities in the two-motor assays were found to be approximately Gaussian distributed, and possessed statistically identical velocities ( $492 \pm 85$  nm/s), compared to those measured in single kinesin assays ( $490 \pm 132$  nm/s) and for the single motor 50 nm scaffold ( $476 \pm 183$  nm/s). This result indicates that this unbinding behavior of the coupled motor scaffold is not biasing the velocity measurements with the presence of large rearward or forward displacements.

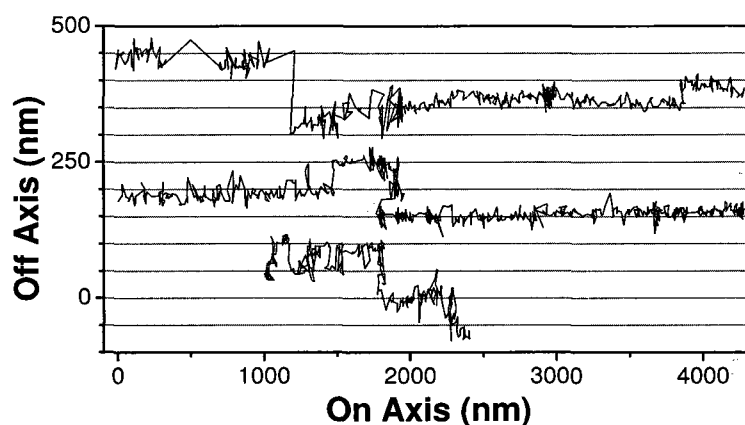


Figure 3.4 : Representative coupled motor traces, with 50 nm axis guides, highlighting displacements characteristic of the engineered assembly joining the two motors.

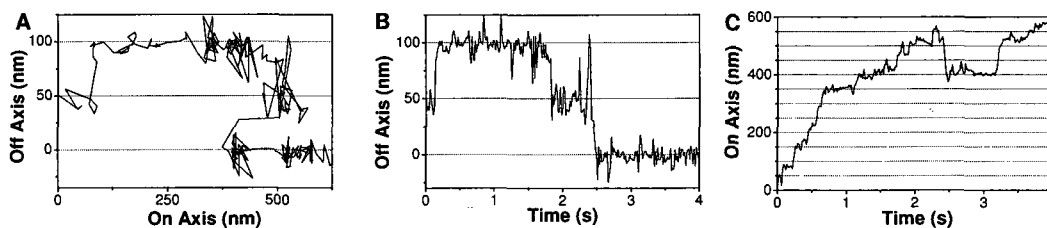


Figure 3.5 : (A) Close-up of a coupled motor trace, showing discrete 50 nm hopping between axonemal filaments. (B) Off- and (C) on-axis components plotted plotted against time.

### 3.0.8 Measurements at Limiting Concentrations of ATP

To further examine how the communication of forces between motors influences their collective transport behavior, QD tracking assays were performed using limiting ATP concentrations (200 nM ATP). The stepping rates of the motors under these conditions are sufficiently slowed to enable single- and coupled-motor step sizes to be measured at 15 millisecond time resolution, allowing assessment of whether coupled-motor molecules exhibit the same step sizes as their single motor counterparts. The trajectories for the single motor distinctly show visible 8 nm stepping behavior analogous to previous reports<sup>16</sup> (see Figure 3.6). The on-axis movement of the single kinesin, Figure 3.8 also clearly shows the 8 nm advancements. The stepping behavior of the coupled motor case was more difficult to interpret because of the lack of obvious stepping, as well as the presence of multiple detachment events (Figure 3.7). Further analysis of on-axis movements was done by generating a pairwise distance histograms that reveal trends in displacements through distributions of distances between two points within a trace. The single motor data (Figure 3.10, panel A) showed a clear periodicity of 8 nm, and contained a dominant peak centered at 0 nm, indicating motors dwells in which the motor maintained the same position between stepping events. The coupled motor stepping data is more ambiguous, lacking the same 8 nm increments in both the on-axis traces (Figure 3.9) and the pairwise distance histogram (Figure 3.10, panel B). This may be due to the steps being obscured by the stretching and relaxation of the assembly between steps, creating the appearance of fractional stepping.<sup>46</sup> There is also a continuance of the large on- and off-axis movements found in the high ATP coupled motor data, which again confirms the influence of the scaffold architecture on the assembly.

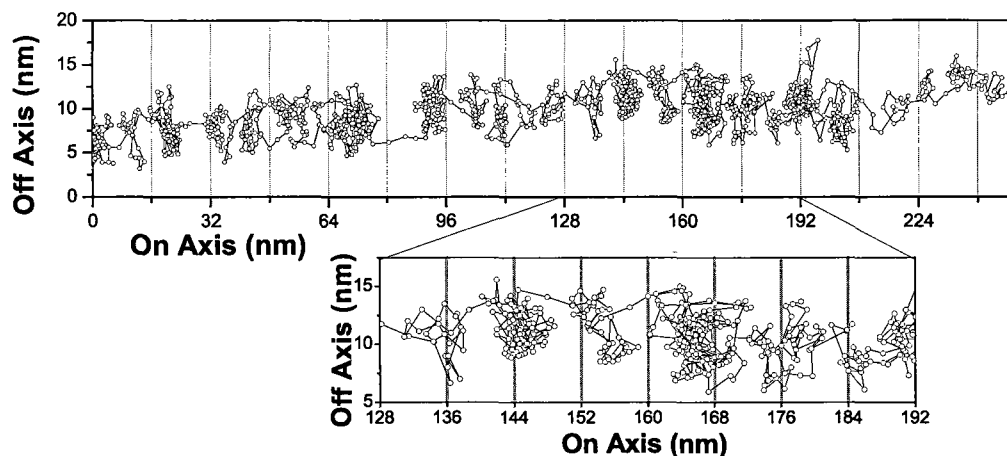


Figure 3.6 : Single motor stepping at low ATP, with 16 nm grid lines. Inset showing enlarged portion of trace with 8 nm grid lines as guides to individual stepping events.

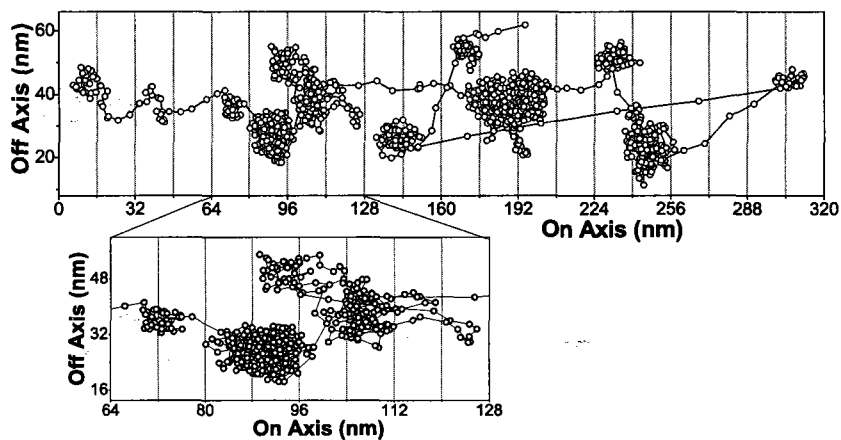


Figure 3.7 : Coupled motor stepping at low ATP. Here, the increased off-axis motion is roughly 3 times than the single motor case. Inset showing enlarged portion of trace with 8 nm grid lines as guides to individual stepping events.

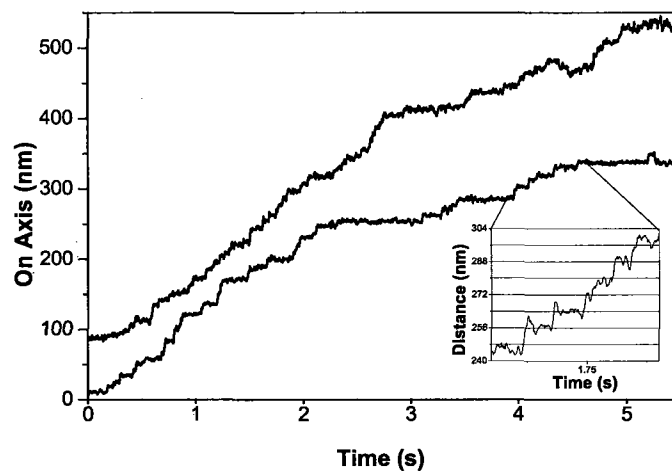


Figure 3.8 : Single motor on-axis traces. Inset shows clear 8 nm displacements, with 8 nm grid lines.

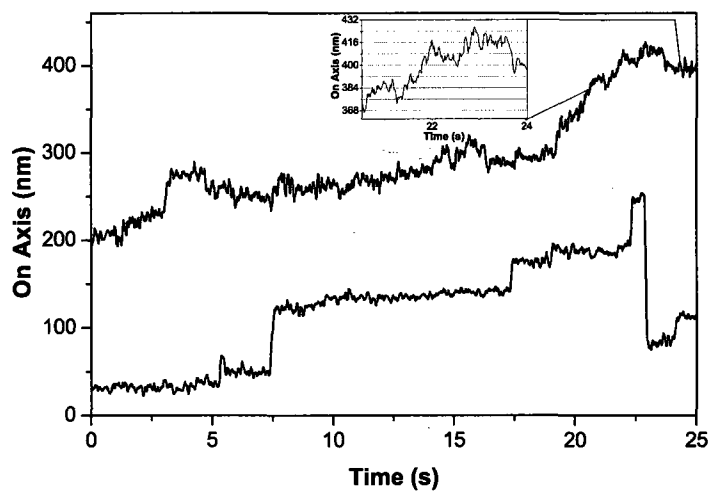


Figure 3.9 : Coupled motor on-axis traces at 200 nM ATP. Inset shows the absence of definitive steps, and large instantaneous displacements.

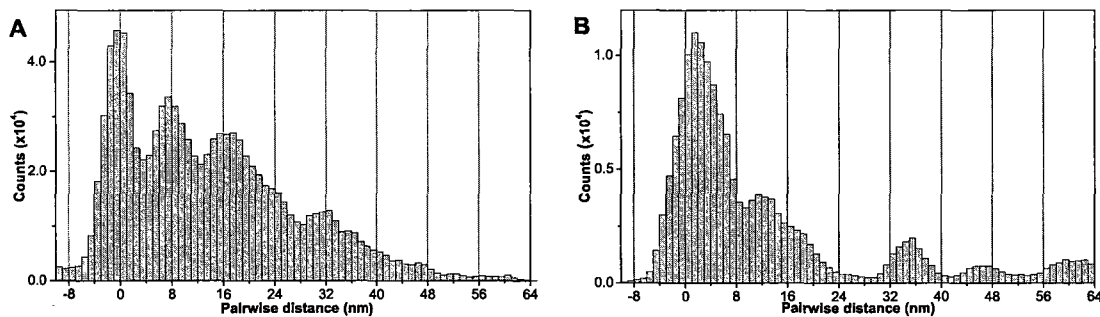


Figure 3.10 : (A) Pairwise histogram showing 8 nm periodicity in single motor displacements. (B) Pairwise distance histogram for coupled motor case, showing loss of stepping resolution, and the emergence of peaks at larger displacements. The large peak at non-zero values also indicates that the assembly is moving between steps, which is interpreted as system relaxation between stepping events.

### 3.1 Transition State Analysis of Coupled Motor Systems

To assess whether cooperative or competitive interactions between motors influence collective run lengths of cargo, run length distribution histograms were constructed for both single- motor and the two-motor assemblies (Figure 3.11), and fit to a transition state model developed by Klumpp et al.<sup>29</sup> Run lengths were taken as the total on-axis distance traveled by the motors during a single encounter with axonemes. Trajectories where a QD moved to the end of an axoneme before detaching or out of the field of view of the microscope were disregarded. Run length distributions for single motors were found to be exponentially distributed and possessed an average run length of  $800 \pm 60$  nm, which agreed well with literature values for the motor.<sup>27,28</sup> The average coupled run length was longer,  $1380 \pm 81$  nm, but significantly shorter than the predicted average run length of  $3.5 \mu\text{m}$ , by the transition state model.

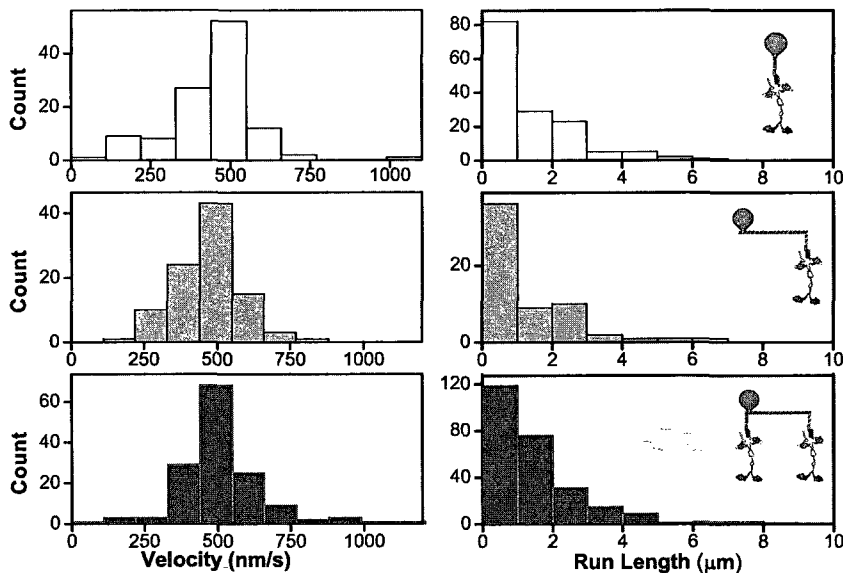


Figure 3.11 : Compiled data for the single molecule experiments. The left column shows the velocity histograms for the single motor (white), single motor on 50 nm scaffold (gray), and coupled motor with scaffold (black). The right column is the run-length data for the corresponding system. Average velocities were statistically similar. The coupled motor run lengths were slightly longer ( $1.4 \mu\text{m}$ ), though not as long as the predicted  $3.5 \mu\text{m}$ .

In the transition state model, the run length distributions can be converted to an expression for first passage time distributions  $\psi_N$  ( $N$  is the total number of motors), using measured velocities. The difference of the single- and coupled- motor constructs were not statistically significant, so it is assumed velocity does not depend on the number of motors engaged in transport. For the single motor case, the first passage time scales as a single exponential:

$$\psi_1 = k_{\text{off}1} e^{-k_{\text{off}1} t} \quad (3.1)$$

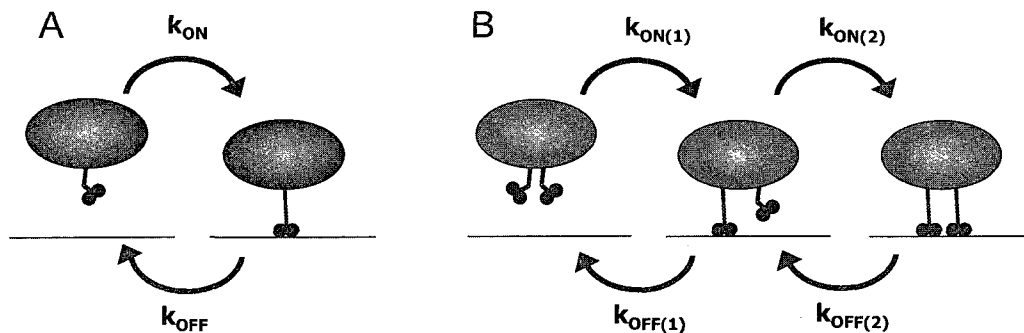


Figure 3.12 : Transition state models for (A) single, and (B) coupled kinesin systems detailing the nomenclature of the kinetic rate constants.

while the expression for first passage time distributions for a two-motor assembly is expressed by:

$$\psi_2 = \frac{k_{off_1}}{2} \left[ \left( 1 - \frac{k_{off_1} + k_{on_2} - k_{off_2}}{R} \right) e^{-\frac{1}{2}(k_{off_1} + k_{on_2} - k_{off_2} - R)t} + \left( 1 + \frac{k_{off_1} + k_{on_2} - k_{off_2}}{R} \right) e^{-\frac{1}{2}(k_{off_1} + k_{on_2} - k_{off_2} + R)t} \right] \quad (3.2)$$

Where  $R \equiv \sqrt{(k_{off_1} + k_{off_2} + k_{on_2})^2 - 4k_{off_1}k_{off_2}}$ ,  $k_{off_1}$  is the rate of complete unbinding of the entire assembly from a single motor attachment,  $k_{off_2}$  is the transition from a two-motor bound state to a single-motor state, and  $k_{on_2}$  is the transition of a single-motor bound state to a two-motor attachment.

This model assumes that motors within complexes do not interact, and step independently with no advantage or cost from other motors in the assembly. Using this assumption, the parameter  $k_{off_2}$  is simply considered twice the value of  $k_{off_1}$  in a two-motor system, because of the equal probability of either motor in a two-motor assembly detaching. Using run length distributions from the single motor data and



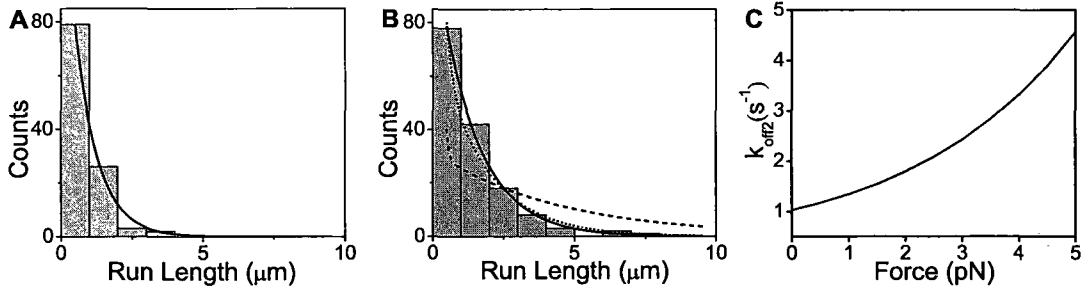


Figure 3.13 : Run length fitting for (A) single and the (B) coupled motor case using the model presented by Klumpp et al. (A) solid black line, single exponential fit to single-motor run lengths. (B) Coupled-motor run-lengths fit with a single exponential (solid line), fit to equation (3.2) with  $k_{on2} = 5 \text{ s}^{-1}$  (dashed line), and single parameter fit of  $k_{on2}$  with  $k_{off2} = 0.61 \text{ s}^{-1}$  (dotted line). (C) Variable  $k_{on2}$  values for a given  $F_C$  when fitting the coupled motor data with a force-dependent unbinding rate  $k_{off2}$  (equation (3.3)).

equation (3.1), the rate at which single motors detach from axonemes was determined. ( $k_{off1} = 0.61 \text{ s}^{-1}$ ;  $k_{off1}/\nu = 1.24 \mu\text{m}^{-1}$ ). This value is only slightly smaller than those previously measured ( $k_{off1} = 1 \text{ s}^{-1}$ ;  $k_{off1}/\nu = 1.25 \mu\text{m}^{-1}$ ),<sup>30</sup> and the run length data fits well to the single-exponential decay, as shown in Figure 3.13, panel A.

The calculated values for  $k_{off1}$  and  $k_{off2}$  (via  $k_{off2} = 2 k_{off1}$ ) were then used to approximate the run length distribution of the two-motor system using a calculated  $k_{on2}$  rate of  $5 \text{ s}^{-1}$  from previous experiments by Koster et al.<sup>86</sup> Using this value in conjunction with equation (3.2) generated a trend (the dashed line in Figure 3.13, panel B), that clearly did not fit the coupled-motor run length histogram. Here, the ratio of  $k_{on2}/k_{off2}$  of 4.1 obtained from the borrowed  $k_{on2}$ , implies a higher probability that both of the motors in the assembly are bound. This leads to longer interaction

times with the microtubule, and the manifestation of a slowly decaying tail in the distribution function at large run lengths. A curious finding was that the coupled system could still be fit to a single exponential, as indicated by the solid line in Figure 3.13, panel B. When the run length data for the coupled motor system was fit to equation (3.2), allowing  $k_{on_2}$  to float, a much closer agreement (dotted line) was obtained. Here, a substantially decreased microtubule binding rate for the second motor is found ( $k_{on_2} = 1.03 \text{ s}^{-1}$ ), that is in agreement with the observation of the single-exponential dependence of the two-motor systems. A slower motor binding rate leads to an increase in the density of assembly states possessing only one microtubule-bound motor, as indicated by a  $< 1$  value for the ratio of the second motor on and off rates ( $k_{on_2}/k_{off_2} = 0.84$ ).

Despite the agreement of the fits described above with our two-motor data, the values obtained for  $k_{off_2}$  using this procedure are inconsistent with the observed microtubule switching behavior found in the two-motor trajectories. As mentioned above, close inspection of individual traces reveals that motors within assemblies frequently detach and rebind microtubules during two-motor runs. A lower bound for the frequency of these events is estimated by determining the number of large and easily identifiable displacements that occur within trajectories ( $4 \mu\text{m}^{-1}$  or  $2 \text{ s}^{-1}$ ). It is also probable that more detachments are occurring, due to the fact that only the motions of the motor nearest to the QD are detected, and that not every dissociation event will result in an observable displacement of the QD. In light of these observations, it is reasonable to assume that  $k_{off_2}$  must be at least as large as  $4 \text{ s}^{-1}$ , making the previous relationship,  $k_{off_2} = 2k_{off_1}$ , incompatible with the new estimate for  $k_{off_2}$ . If  $k_{off_2} > 2k_{off_1}$  there must be interaction between the motors in the two-motor bound state

that enhances the detachment rate, favoring single-motor transport. It is possible that, when both motors are bound, asynchronous stepping stretches the connecting linkages, causing an accumulation of strain in the system that is only relaxed when a motor releases from the microtubule. This effect would not alter binding of the second motor ( $k_{on_2}$ ), but would lead to an increase in the transition to the single-motor state (higher rates of  $k_{off_2}$ ). The dependence of motor unbinding on forces can be approximated by:

$$k_{off_2} = 2k_{off_1} e^{\frac{F_C}{F_D}} \quad (3.3)$$

Where  $F_C$  is the counter force developed within motor assemblies and  $F_D$  is the ‘detachment’ force,  $F_D = k_B T/d$ , dependent on Boltzmann’s constant  $k_B$ , the temperature  $T$ , and distance of a detached motor from the microtubule  $d$ . While  $F_D$  is called a detachment force, it is actually a scaling force determined experimentally to be 3 pN.<sup>32</sup>

Fitting the run length histogram to equation (3.2) and using the new expression for the unbinding rate  $k_{off_2}$  produces a range of potential values for  $k_{on_2}$  for a given counter force (see Figure 3.13, panel C,  $k_{on_2}$  vs.  $F_C$ ). While it is not possible with the current experimental setup to determine the instantaneous forces between the motors, the counter forces within the system will fluctuate rapidly during transport. The spring constant for the motor linkages in the coupled motor system was determined to be  $\approx 0.1$  pN nm<sup>-1</sup> by optical force spectroscopy (D. K. Jamison, *unpublished data*). This means that for each asynchronous step, 0.8 pN of strain ( $F_C$ ) is generated between the motors. The detachment rate  $k_{off_2}$  is affected exponentially by this value, and high rates of detachment could be generated by low average forces between the coupled motors. While measuring the instantaneous forces in the system would give

a more definitive answer, the single-exponential fit of the coupled motor run lengths, and increased unbinding rate imply internal struggle within the motor assembly.

### 3.1.1 Negative Interference in Coupled Kinesin

The results of the study conclude that, under low loads, the average transport state in multi-kinesin assemblies utilizes a subset of the total available motors, due to negative interference between coupled motors. It is proposed that intermotor strain between elastic linkage enhances the transition of coupled kinesin to a single-motor bound state. Due to the stochastic nature of kinesin stepping,<sup>49</sup> the duration of the individual steps is short when compared to the total time spent bound to the microtubule, allowing for asynchronous stepping and the accrual of intermotor forces that are only relaxed through motor dissociation. Although the average run length of two coupled motors was found to be longer than that of single motors, these forces affect transport at zero load by lowering the average lifetime of states with two motors bound to microtubules. Transition state modeling of the coupled motor run length data yields a kinetic ratio of  $k_{on2}/k_{off2} < 1$ , which supports the premise of a predominantly single-motor state of attachment to the microtubule. The exchange between motor-bound configurations still results in increased effective interaction times with the microtubules, and longer run lengths, but overall, negative interference causes motor assemblies to effectively behave like a single motor with an attenuated detachment rate, or increased processivity. This picture of collective motility explains recent observations that the run lengths of vesicular cargos are not substantially affected by reduced levels of kinesin expression.<sup>87</sup> Negative interference would mask signs of transport by multiple motors, making varying-size systems of kinesins indis-

tinguishable.

Determining the precise magnitude of internal force within motor assemblies still requires further investigation, particularly through direct measurement of the microtubule binding and unbinding rates to confirm the relationship between the kinetic rate constants of the coupled-motor systems. Measuring the assemblies under applied load will also aid the understanding of the interplay between intermotor attachments and compliance, and their effect on the kinetic rates of the coupled kinesin system. The synthetic approach and the modularity of the self-assembling two-motor scaffold will be a keystone in making the examination of these aspects of collective motility possible.

## **3.2 Methods to Assay Coupled Motor Activity**

### **3.2.1 Assay Conditions**

Prior to single motor assays, the conjugate-linker was hybridized to the 5-bio strand (see table 2.11 in the previous chapter) overnight, to present a biotin molecule for streptavidin-coated QD ( attachment emission maximum at  $655\lambda$ , Invitrogen). The motors were then incubated 4:1 for 20 minutes with the biotin conjugate, added 4:1 QD to conjugate for 10 minutes, and then used for imaging as described below. Schematics for both the single and coupled motor assays are shown in Figure 3.2.

The preparation for the coupled motor assay begins with the annealment of the single biotin 50 nm scaffold. The strands 1, 3, 5-bio-11-10, and 2-9-8 are combined and annealed as described in the previous chapter. The assembled 50 nm scaffold is

then combined 1:2.5 with the conjugate-linker overnight at 4°C. The motor is then incubated 4:1 with the 50 nm partial assembly for 20 minutes, then combined 1:4 with the QD (a diagram of assembly is shown in Figure 3.1), and imaged as described below.

To verify that the scaffold was not participating in microtubule binding, a single motor 50 nm scaffold assay was performed, in which one of the two single-stranded overhangs was replaced with a ‘blunt’ strand. For the single motor DNA attachment assay, the strands 1, 3, 5-bio-11-10, and 2-blunt-9-8 were constructed as described in the previous chapter, and the assay conditions were identical to the coupled motor assay.

Single quantum dot tracking assays were performed at room temperature using a low ionic strength buffer (0.25 mg/mL  $\alpha$ -casein BRB12 supplemented with 143 mM  $\beta$ -mercaptoethanol, 40 mM glucose, 10 mM MgCl<sub>2</sub> and oxygen scavenging solution composed of 70 mg/mL glucose oxidase and 3.3 mg/mL catalase). Single molecule assays began with the introduction of sea urchin axonemes in BRB12 (12 mM PIPES, 2 mM MgCl<sub>2</sub>, 2 mM EGTA) into a flow chamber formed by a glass slide, a coverslip, and dual-sided tape. Immediately afterwards, the chamber was exchanged with a solution containing 1 mg/mL  $\alpha$ -casein in BRB12 to orient the axonemes and wash out unbound filaments. For high ATP measurements, the final wash was 1 nM of the QD/motor complex in imaging solution (BRB12 (12 mM K-PIPES, 2 mM MgCl<sub>2</sub>, 1 mM EGTA) with 2 mM ATP, 1X Gloxy, 40 mM glucose, 1.43 mM  $\beta$ ME, 10 mM MgCl<sub>2</sub>), before the chamber was sealed and imaged. Low ATP conditions for step size analysis differed slightly, in that, the QD/motor complex was perfused in without ATP, allowed to bind for 5 minutes, and then imaging buffer containing 200 nM ATP

and an ATP regeneration system (2 units per mL creatine kinase, 2 mM creatine phosphate) was introduced before sealing the chamber.

### 3.2.2 Microscopy and Data Analysis

All fluorescence measurements were taken on an inverted, objective-based total internal reflection fluorescence (TIRF) microscope outfitted with piezo stages to control the positioning of the objective and sample stages (Piezajena and Mad City Labs, respectively). These stages were mounted onto an aluminium housing designed to minimize sample drift. The laser (20 mW, 488 nm) was fiber-coupled to the optical table to remove vibrations induced by its fan. The remaining drift ( $\approx 6$  nm/min) was removed during data processing via surface-immobilized quantum dots (QDs) which served as fiducial markers. The microscope also incorporates a 60 X 1.45 NA objective (Nikon) and EMCCD camera (Andor). Typically, 4500 photons could be detected from a QD over 15 ms with a point-spread function (PSF) width of 225 nm, yielding an uncertainty in the QD's measured position of 2-3 nm.<sup>16</sup> Mobile QDs tended towards the upper bound of this range, due to the decreased intensity of the evanescent excitation field of the TIRF microscope with increasing distance from the coverslip surface. A QD's centroid position was determined *via* the non-linear least squares fit of its PSF to a two-dimensional Gaussian distribution. The process of finding and fitting a QD's PSF through a time series of images was automated through custom software written in MatLab (MathWorks, Natick, MA). The resulting localized positions were superimposed upon the image stack to allow for manual verification.

## Chapter 4

### Conclusion

#### 4.1 Conclusion

Within this work a self-assembly approach is used to build coupled complexes of kinesin motors on rigid DNA scaffolds with direct control over intermotor spacing and the stiffness of the intermotor attachments. The transport properties of the motor systems were then measured using fluorescence microscopy *in vitro*. It was determined that the average velocity was statistically indistinguishable than that of the single motor, and the average run length slightly larger, but less than estimated for a system of non-interacting motors. This result, when combined with the observation of enhanced partial detachments and protofilament switching behavior, lead to the hypothesis that intermotor strain is creating enhanced transition rates to a single-motor attachment state. This negative interference between motors means that even though multiple motors are present on a cargo, asynchronous stepping will create forces that quickly transition the complex to a single motor-attached state.



## 4.2 Negative Interference: Continued Studies of the Two Motor Case

### 4.2.1 Discrete Transition State Modeling of Coupled Motor Transport

A further refinement of the transition state model used to analyze the run length data presented in Chapter 2 (pp.14) was created in which a ‘discrete rate transition state model’ accounts for the mechanical and structural nuances in the binding and stepping transitions between distinct microtubule-bound configurations (termed ‘microstates’) of a multiple motor system. Strain in the system is a function of the linker stiffness  $\kappa$  and the distance that the linkages are stretched from equilibrium. The stiffer the linkages (larger  $\kappa$ ) the greater the transmission of strain, the less separation distance the system will tolerate, the faster the rate of partial detachment, and the lower the rate of re-attachment into high-strain microstates. The rate of return to the two motor attachment state is particularly sensitive to strain and decreases precipitously with linker stiffness. Once the kinesin binds the microtubule, there are three possible outcomes: the kinesin begins an extended run, undergoes a pausing event (possibly waiting for ATP or encountering some sort of microtubule-based obstacle),<sup>88</sup> or detaches completely from the microtubule. Due to the stochastic nature of the enzymes it is highly unlikely that the presence of multiple motors will induce synchronous behavior. Within a coupled motor system, a single motor binds and begins to step toward the plus-end of the microtubule. If the second motor in the complex is not moving as well, forces are communicated through the assembly linkages. This strain that develops between the motors can only be satisfied by closing the distance between the motors, or partially detaching by releasing a single motor from the microtubule (See Figure 4.1). Therefore, the exhibited negative interference is the

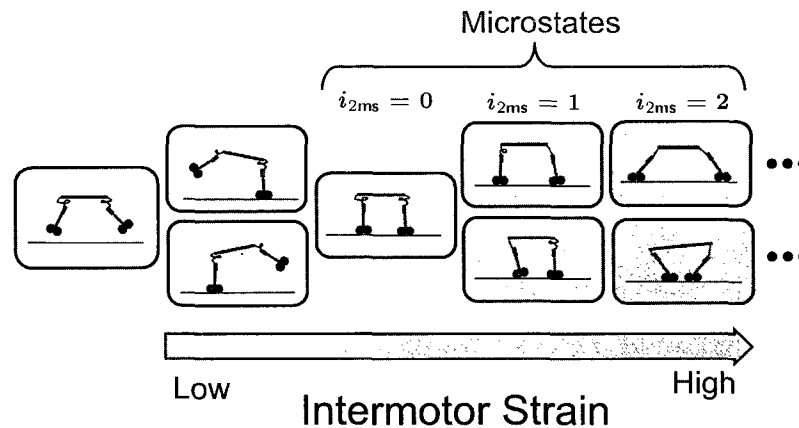


Figure 4.1 : Diagram showing the generation of strain in coupled motor complexes by asynchronous stepping. Once the motor complex attaches by both motors, it can enter a series of ‘microstates’, dependent on the number of uncoordinated steps. Degenerate microstates are enumerated with the index  $i_{2ms}$ . While in states  $i_{2ms} > 0$  the rate of transition to the single motor case becomes higher due to the release of strain.

product of forces generated by uncoordinated steps between the motors. Within the two motor bound state, each ‘microstate’ ( $i_{2ms}$ ) is defined by a single asynchronous step. A single step by the leading motor or lagging motor, without response from the partner, results in a degenerate state  $i_{2ms}=1$ . If the partner motors in either case close the distance the microstate returns to  $i_{2ms}=0$ , and successive asynchronous steps result in values of  $i_{2ms} + 1$  for each step.

It is generally expected that average run lengths will increase with increasing motor number, but the discrete transition state model suggests that gain in run length through added motor participation is lessened by intermotor strain that reduces microtubule binding and increases detachment. It was also found that even if the motors step synchronously that the gains in run length were not increased, primarily due to

the decrease in microtubule binding that leads to the predominance of the single motor transport state.

#### **4.2.2 Coupled Motor Response to Applied Load**

Optical trapping experiments recently conducted that utilize the same self-assembling materials to generate coupled kinesin complexes show instances of increased force generation ( $> 17$  pN) and higher velocities under load than single kinesin, but at applied loads below kinesin's stall force, the complex essentially behaves as a single motor. There is also evidence of enhanced detachment at low forces. This heightened detachment is interpreted as due to the additive force that the lagging motor applies to the leading motor. When the leading motor is traveling away from the center of the trap forces increase, and when the additive forces of the trap and lagging motor equal the stall force, the detachment rate increases dramatically, with the overall effect of reducing the transport efficiency of the coupled motors.

### **4.3 Future Directions**

#### **4.3.1 Increased Elastic Compliance**

The discrete state transition model predicts that the intermotor strain is directly impacted by the compliance. Rigid motor connections play a role in altering the binding kinetics of motors in groups, creating a situation where motors are less likely to bind into high-energy strained states. Assays could be developed that study mechanical response to changes in linker compliance, using the inherent modularity of the convergent self-assembling materials to increase of the elasticity of the intermotor connections. In an assay with longer elastin polymers, a possible outcome is that the

system would be less sensitive to strain, and exhibit increased run lengths and force production.

#### 4.3.2 Dynamic Motor Attachments to Cargo

In a coupled motor assembly with both motors bound to microtubules and applied load, geometric modeling predicts that the progression of the rear motor increases its assumption of load and imposes a tangential force upwards through the linkages on the leading motor. This lifts the leading motor in an unnatural angle, relative to single motor transport, increasing the rate of detachment. The resting angle of the kinesin during transport may be important for holding the motor in a preferred, load-bearing (or strain gating), conformation. The result is a case analogous to the mechanical cycle of kinesin; conformational change in the leading head upon the binding of ATP pulls the lagging head up and forward, increasing its detachment rate.<sup>89</sup>

The rigid motor anchoring in the system may be applying forces that are not present in natural transport scenarios. Motor attachment conventions that more closely mimic the natural associations to endogenous particles should be investigated. Natural cargos, like liposomes, have surfaces have been described as ‘fluidlike’, and resist tangential forces.<sup>33</sup> Motors must cluster to contribute to the normal force propelling transport. In such an experiment, a motor could bind to the microtubule, and a second motor could diffuse freely within the lipid membrane until it is within range of the surface. Upon binding, the second motor would not apply a tangential load, but accelerate to the point at which the first motor is hauling the cargo, and apply additive force. Once the second motor arrives the load is then presumably spread equally among the motors, reducing the effective load per motor, presumably increasing the observed velocity against load.

### 4.3.3 Creating Bidirectional Complexes

The majority of axonal transport is done by groups of the oppositely directional motors dynein and kinesin, which exhibit complex bidirectional behavior, as in the case of mitochondrial transport through axonal processes. Experiments have shown that transported mitochondria reach equilibrium in their positions within the optic nerves of rats, and cease to progress substantially in either direction.<sup>90</sup> This suggests that the average distribution of organelles like mitochondria, may be regulated by bidirectional transport. To further support this idea, the upregulation of kinesin gene expression has been linked to cardiovascular stresses, where it is necessary to distribute mitochondria throughout the heart tissue, based on metabolic demand.<sup>91</sup> In neurons, mitochondria are needed in the far extremities to produce ATP to keep transport going. It is known that kinesin and dynein are the primary movers of these organelles, and that during transport there are frequent pauses and retrograde phases. It may be possible that the system is sensing gradients in ATP. In regions of low ATP concentration the anterograde travel stalls, allowing the ATP concentration to increase from the mitochondrial release of ATP. When the mitochondrial energy generation begins to fail, the retrograde transport initiates, taking the organelle back for degradation. In this manner, the bidirectional transport generates an even concentration of ATP in the axon.<sup>92</sup> It may be possible that, due to the multiple ATP binding sites,<sup>93</sup> dynein is more sensitive to ATP concentration and activates retrograde transport at low ATP levels.<sup>94,95</sup>

Much could be learned about bidirectional transport mechanics by creating artificial assemblies of these motors. Currently, the study of dynein is limited due to its large size, poor recombinant expression, and difficult purification from tissue. Without the ability to recombinantly express fusion proteins with dynein, there are

limitations to modifications that can be employed to generate assemblies analogous to coupled kinesin complexes presented in this work. A possible solution to this problem is the development of affinity tags that can be used to group dynein within cells. For now, transferring the self-assembly technology into the cells is the chief hurdle.

## Bibliography

- [1] Gennerich, A. and Schild, D. Finite-particle tracking reveals submicroscopic-size changes of mitochondria during transport in mitral cell dendrites. *Phys. Biol.* **3**(1), 45–53, Mar (2006).
- [2] Trejo, H. E., Lecuona, E., Grillo, D., Szleifer, I., Nekrasova, O. E., Gelfand, V. I., and Sznajder, J. I. Role of kinesin light chain-2 of kinesin-1 in the traffic of na,k-atpase-containing vesicles in alveolar epithelial cells. *FASEB J.* **24**(2), 374–82, Feb (2010).
- [3] Roy, S., Zhang, B., Lee, V. M.-Y., and Trojanowski, J. Q. Axonal transport defects: a common theme in neurodegenerative diseases. *Acta. Neuropathol.* **109**(1), 5–13, Jan (2005).
- [4] Hirokawa, N. and Takemura, R. Molecular motors in neuronal development, intracellular transport and diseases. *Curr. Opin. Neurobiol.* **14**(5), 564–73, Oct (2004).
- [5] Martin, M., Iyadurai, S. J., Gassman, A., Gindhart, J. G., Hays, T. S., and Saxton, W. M. Cytoplasmic dynein, the dynactin complex, and kinesin are interdependent and essential for fast axonal transport. *Mol. Biol. Cell* **10**(11), 3717–28, Nov (1999).
- [6] Muresan, V., Godek, C. P., Reese, T. S., and Schnapp, B. J. Plus-end motors

- override minus-end motors during transport of squid axon vesicles on microtubules. *J. Cell. Biol.* **135**(2), 383–97, Oct (1996).
- [7] Stokin, G. B. and Goldstein, L. S. B. Axonal transport and alzheimer's disease. *Annu. Rev. Biochem.* **75**, 607–27, Jan (2006).
- [8] Chevalier-Larsen, E. and Holzbaaur, E. L. F. Axonal transport and neurodegenerative disease. *Biochim. Biophys. Acta* **1762**(11-12), 1094–108, Jan (2006).
- [9] Morfini, G., Pigino, G., Opalach, K., Serulle, Y., Moreira, J. E., Sugimori, M., Llinás, R. R., and Brady, S. T. 1-methyl-4-phenylpyridinium affects fast axonal transport by activation of caspase and protein kinase c. *Proc. Natl. Acad. Sci. USA* **104**(7), 2442–7, Feb (2007).
- [10] Ermolayev, V., Cathomen, T., Merk, J., Friedrich, M., Härtig, W., Harms, G. S., Klein, M. A., and Flechsig, E. Impaired axonal transport in motor neurons correlates with clinical prion disease. *PLoS Pathog.* **5**(8), e1000558, Aug (2009).
- [11] Gross, S. P., Vershinin, M., and Shubeita, G. T. Cargo transport: two motors are sometimes better than one. *Curr. Biol.* **17**(12), R478–86, Jun (2007).
- [12] Navone, F., Niclas, J., Hom-Booher, N., Sparks, L., Bernstein, H. D., McCaffrey, G., and Vale, R. D. Cloning and expression of a human kinesin heavy chain gene: interaction of the cooh-terminal domain with cytoplasmic microtubules in transfected cv-1 cells. *J. Cell. Biol.* **117**(6), 1263–75, Jun (1992).
- [13] Ashkin, A., Schütze, K., Dziedzic, J. M., Euteneuer, U., and Schliwa, M. Force generation of organelle transport measured in vivo by an infrared laser trap. *Nature* **348**(6299), 346–8, Nov (1990).



- [14] Goldstein, L. S. B. and Philp, A. V. The road less traveled: emerging principles of kinesin motor utilization. *Annu. Rev. Cell. Dev. Biol.* **15**, 141–83, Jan (1999).
- [15] Li, H., DeRosier, D. J., Nicholson, W. V., Nogales, E., and Downing, K. H. Microtubule structure at 8 Å resolution. *Structure* **10**(10), 1317–28, Oct (2002).
- [16] Yildiz, A., Tomishige, M., Vale, R. D., and Selvin, P. R. Kinesin walks hand-over-hand. *Science* **303**(5658), 676–8, Jan (2004).
- [17] Guydosh, N. R. and Block, S. M. Direct observation of the binding state of the kinesin head to the microtubule. *Nature* **461**(7260), 125–8, Sep (2009).
- [18] Kozielski, F., Sack, S., Marx, A., Thormählen, M., Schönbrunn, E., Biou, V., Thompson, A., Mandelkow, E. M., and Mandelkow, E. The crystal structure of dimeric kinesin and implications for microtubule-dependent motility. *Cell* **91**(7), 985–94, Dec (1997).
- [19] Tuszynski, J., Brown, J., Crawford, E., Carpenter, E., Nip, M., Dixon, J., and Sataric, M. Molecular dynamics simulations of tubulin structure and calculations of electrostatic properties of microtubules. *Math. Comput. Model.* **41**(10), 1055–1070, Jan (2005).
- [20] Yonekura, H., Nomura, A., Ozawa, H., Tatsu, Y., Yumoto, N., and Uyeda, T. Q. P. Mechanism of tail-mediated inhibition of kinesin activities studied using synthetic peptides. *Biochem. Biophys. Res. Commun.* **343**(2), 420–7, May (2006).
- [21] Dietrich, K. A., Sindelar, C. V., Brewer, P. D., Downing, K. H., Cremo, C. R., and Rice, S. E. The kinesin-1 motor protein is regulated by a direct interaction of its head and tail. *Proc. Natl. Acad. Sci. USA* **105**(26), 8938–43, Jul (2008).

- [22] Verhey, K. J. and Rapoport, T. A. Kinesin carries the signal. *Trends Biochem. Sci.* **26**(9), 545–50, Sep (2001).
- [23] Hammond, J. W., Griffin, K., Jih, G. T., Stuckey, J., and Verhey, K. J. Cooperative versus independent transport of different cargoes by kinesin-1. *Traffic* **9**(5), 725–41, May (2008).
- [24] Verhey, K. J., Meyer, D. E., Deehan, R., Blenis, J., Schnapp, B. J., Rapoport, T. A., and Margolis, B. Cargo of kinesin identified as jip scaffolding proteins and associated signaling molecules. *J. Cell. Biol.* **152**(5), 959–70, Mar (2001).
- [25] Hirokawa, N. Kinesin and dynein superfamily proteins and the mechanism of organelle transport. *Science* **279**(5350), 519–26, Jan (1998).
- [26] Miller, R. H. and Lasek, R. J. Cross-bridges mediate anterograde and retrograde vesicle transport along microtubules in squid axoplasm. *J. Cell. Biol.* **101**(6), 2181–93, Dec (1985).
- [27] Case, R. B., Pierce, D. W., Hom-Booher, N., Hart, C. L., and Vale, R. D. The directional preference of kinesin motors is specified by an element outside of the motor catalytic domain. *Cell* **90**(5), 959–66, Sep (1997).
- [28] Thorn, K. S., Ubersax, J. A., and Vale, R. D. Engineering the processive run length of the kinesin motor. *J. Cell. Biol.* **151**(5), 1093–100, Nov (2000).
- [29] Klumpp, S. and Lipowsky, R. Cooperative cargo transport by several molecular motors. *Proc. Natl. Acad. Sci. USA* **102**(48), 17284–9, Nov (2005).
- [30] Beeg, J., Klumpp, S., Dimova, R., Gracià, R. S., Unger, E., and Lipowsky, R.

- Transport of beads by several kinesin motors. *Biophys. J.* **94**(2), 532–41, Jan (2008).
- [31] Vershinin, M., Carter, B. C., Razafsky, D. S., King, S. J., and Gross, S. P. Multiple-motor based transport and its regulation by tau. *Proc. Natl. Acad. Sci. USA* **104**(1), 87–92, Jan (2007).
- [32] Schnitzer, M. J., Visscher, K., and Block, S. M. Force production by single kinesin motors. *Nat. Cell Biol.* **2**(10), 718–23, Oct (2000).
- [33] Campas, O., Leduc, C., Bassereau, P., Casademunt, J., Joanny, J.-F., and Prost, J. Coordination of kinesin motors pulling on fluid membranes. *Biophys. J.* **94**(12), 5009–17, Jun (2008).
- [34] Sims, P. A. and Xie, X. S. Probing dynein and kinesin stepping with mechanical manipulation in a living cell. *Chem. Phys. Chem.* **10**(9-10), 1511–6, Jul (2009).
- [35] Shtridelman, Y., Cahyuti, T., Townsend, B., DeWitt, D., and Macosko, J. C. Force-velocity curves of motor proteins cooperating in vivo. *Cell Biochem. Biophys.* **52**(1), 19–29, Jan (2008).
- [36] Levi, V., Serpinskaya, A. S., Gratton, E., and Gelfand, V. I. Organelle transport along microtubules in xenopus melanophores: evidence for cooperation between multiple motors. *Biophys. J.* **90**(1), 318–27, Jan (2006).
- [37] Macosko, J. C., Newbern, J. M., Rockford, J., Chisena, E. N., Brown, C. M., Holzwarth, G. M., and Milligan, C. E. Fewer active motors per vesicle may explain slowed vesicle transport in chick motoneurons after three days in vitro. *Brain Res.* **1211**, 6–12, May (2008).

- [38] Goldstein, L. S. B. and Yang, Z. Microtubule-based transport systems in neurons: the roles of kinesins and dyneins. *Annu. Rev. Neurosci.* **23**, 39–71, Jan (2000).
- [39] Ling, S.-C., Fahrner, P. S., Greenough, W. T., and Gelfand, V. I. Transport of drosophila fragile x mental retardation protein-containing ribonucleoprotein granules by kinesin-1 and cytoplasmic dynein. *Proc. Natl. Acad. Sci. USA* **101**(50), 17428–33, Dec (2004).
- [40] Cai, D., McEwen, D. P., Martens, J. R., Meyhofer, E., and Verhey, K. J. Single molecule imaging reveals differences in microtubule track selection between kinesin motors. *Plos Biol.* **7**(10), e1000216, Oct (2009).
- [41] Dunn, S., Morrison, E. E., Liverpool, T. B., Molina-Paris, C., Cross, R. A., Alonso, M. C., and Peckham, M. Differential trafficking of kif5c on tyrosinated and detyrosinated microtubules in live cells. *J. Cell Sci.* **121**(7), 1085–1095, Mar (2008).
- [42] Dixit, R., Ross, J. L., Goldman, Y. E., and Holzbaur, E. L. F. Differential regulation of dynein and kinesin motor proteins by tau. *Science* **319**(5866), 1086–9, Feb (2008).
- [43] Sato-Yoshitake, R., Yorifuji, H., Inagaki, M., and Hirokawa, N. The phosphorylation of kinesin regulates its binding to synaptic vesicles. *J. Biol. Chem.* **267**(33), 23930–6, Nov (1992).
- [44] Welte, M. A. Bidirectional transport along microtubules. *Curr. Biol.* **14**(13), R525–37, Jul (2004).
- [45] Gross, S. P., Welte, M. A., Block, S. M., and Wieschaus, E. F. Coordination of opposite-polarity microtubule motors. *J. Cell. Biol.* **156**(4), 715–24, Feb (2002).

- [46] Leduc, C., Ruhnaw, F., Howard, J., and Diez, S. Detection of fractional steps in cargo movement by the collective operation of kinesin-1 motors. *Proc. Natl. Acad. Sci. USA* **104**(26), 10847–52, Jun (2007).
- [47] Gagliano, J., Walb, M., Blaker, B., Macosko, J. C., and Holzwarth, G. M. Kinesin velocity increases with the number of motors pulling against viscoelastic drag. *Eur. Biophys. J. AOP*, Nov (2009).
- [48] Kunwar, A., Vershinin, M., Xu, J., and Gross, S. P. Stepping, strain gating, and an unexpected force-velocity curve for multiple-motor-based transport. *Curr. Biol.* **18**(16), 1173–83, Aug (2008).
- [49] Bieling, P., Telley, I. A., Piehler, J., and Surrey, T. Processive kinesins require loose mechanical coupling for efficient collective motility. *EMBO Rep.* **9**(11), 1121–1127, Nov (2008).
- [50] Leduc, C., Campas, O., Zeldovich, K. B., Roux, A., Jolimaître, P., Bourel-Bonnet, L., Goud, B., Joanny, J.-F., Bassereau, P., and Prost, J. Cooperative extraction of membrane nanotubes by molecular motors. *Proc. Natl. Acad. Sci. USA* **101**(49), 17096–101, Dec (2004).
- [51] Block, S. M., Goldstein, L. S. B., and Schnapp, B. J. Bead movement by single kinesin molecules studied with optical tweezers. *Nature* **348**(6299), 348–52, Nov (1990).
- [52] Mallik, R., Carter, B. C., Lex, S. A., King, S. J., and Gross, S. P. Cytoplasmic dynein functions as a gear in response to load. *Nature* **427**(6975), 649–52, Feb (2004).

- [53] Gennerich, A., Carter, A. P., Reck-Peterson, S. L., and Vale, R. D. Force-induced bidirectional stepping of cytoplasmic dynein. *Cell* **131**(5), 952–65, Nov (2007).
- [54] Hendricks, A. G., Epureanu, B. I., and Meyhofer, E. Cooperativity of multiple kinesin-1 motors mechanically coupled through a shared load. *Physica D* **238**(6), 677–686, Jan (2009).
- [55] Jülicher, F. and Prost, J. Cooperative molecular motors. *Phys. Rev. Lett.* **75**(13), 2618–2621, Sep (1995).
- [56] Holzbauer, E. L. F. and Goldman, Y. E. Coordination of molecular motors: from in vitro assays to intracellular dynamics. *Curr. Opin. Cell Biol.* **22**(1), 4–13, Feb (2010).
- [57] Constantinou, P. E. and Diehl, M. R. The mechanochemistry of integrated motor protein complexes. *J. Biomech.* **43**(1), 31–7, Jan (2010).
- [58] Jørgensen, K., Rasmussen, A. V., Morant, M., Nielsen, A. H., Bjarnholt, N., Zagrobelny, M., Bak, S., and Møller, B. L. Metabolon formation and metabolic channeling in the biosynthesis of plant natural products. *Curr. Opin. Plant Biol.* **8**(3), 280–91, Jun (2005).
- [59] Marahiel, M. A. Working outside the protein-synthesis rules: insights into non-ribosomal peptide synthesis. *J. Pept. Sci.* **15**(12), 799–807, Dec (2009).
- [60] Epshtein, V. and Nudler, E. Cooperation between rna polymerase molecules in transcription elongation. *Science* **300**(5620), 801–5, May (2003).
- [61] Jung, G. Y. and Stephanopoulos, G. A functional protein chip for pathway

- optimization and in vitro metabolic engineering. *Science* **304**(5669), 428–31, Apr (2004).
- [62] Niemeyer, C. M., Koehler, J., and Wuerdemann, C. Dna-directed assembly of bienzymic complexes from in vivo biotinylated nad(p)h:fmn oxidoreductase and luciferase. *ChemBiochem* **3**(2-3), 242–5, Mar (2002).
- [63] Diehl, M. R., Zhang, K., Lee, H. J., and Tirrell, D. A. Engineering cooperativity in biomotor-protein assemblies. *Science* **311**(5766), 1468–71, Mar (2006).
- [64] Rothmund, P. W. K. Folding dna to create nanoscale shapes and patterns. *Nature* **440**(7082), 297–302, Mar (2006).
- [65] Douglas, S. M., Dietz, H., Liedl, T., Högberg, B., Graf, F., and Shih, W. M. Self-assembly of dna into nanoscale three-dimensional shapes. *Nature* **459**(7245), 414–8, May (2009).
- [66] Seeman, N. C. De novo design of sequences for nucleic acid structural engineering. *J. Biomol. Struct. Dyn.* **8**(3), 573–81, Dec (1990).
- [67] Moll, J. R., Ruvinov, S. B., Pastan, I., and Vinson, C. Designed heterodimerizing leucine zippers with a range of p<sub>is</sub> and stabilities up to 10<sup>(-15)</sup> m. *Protein Sci.* **10**(3), 649–55, Mar (2001).
- [68] Crick, F. The packing of alpha-helices: simple coiled-coils. *Acta Crystallogr.* **6**(8-9), 689–697 (1953).
- [69] Urry, D. W., Hugel, T., Seitz, M., Gaub, H. E., Sheiba, L., Dea, J., Xu, J., and Parker, T. Elastin: a representative ideal protein elastomer. *Philos. Trans. R. Soc. Lond., B, Biol. Sci.* **357**(1418), 169–84, Feb (2002).

- [70] Urry, D. Physical chemistry of biological free energy transduction as demonstrated by elastic protein-based polymers. *J. Phys. Chem. B* **101**(51), 11007–11028, Dec (1997). doi: 10.1021/jp972167t.
- [71] Uto, I., Ishimatsu, T., Hirayama, H., Ueda, S., Tsuruta, J., and Kambara, T. Determination of urinary tamm-horsfall protein by elisa using a maleimide method for enzyme-antibody conjugation. *J. Immunol. Methods* **138**(1), 87–94, Apr (1991).
- [72] Seitz, A. and Surrey, T. Processive movement of single kinesins on crowded microtubules visualized using quantum dots. *EMBO J.* **25**(2), 267–77, Jan (2006).
- [73] Schweller, R. M., Constantinou, P. E., Frankel, N. W., Narayan, P., and Diehl, M. R. Design of dna-conjugated polypeptide-based capture probes for the anchoring of proteins to dna matrices. *Bioconjug. Chem.* **19**(12), 2304–7, Dec (2008).
- [74] Svoboda, K. and Block, S. M. Biological applications of optical forces. *Annu. Rev. Biophys. Biomol. Struct.* **23**, 247–85, Jan (1994).
- [75] Berliner, E., Mahtani, H. K., Karki, S., Chu, L. F., Cronan, J. E., and Gelles, J. Microtubule movement by a biotinylated kinesin bound to streptavidin-coated surface. *J. Biol. Chem.* **269**(11), 8610–8615, Mar (1994).
- [76] Meyer, D. E. and Chilkoti, A. Genetically encoded synthesis of protein-based polymers with precisely specified molecular weight and sequence by recursive directional ligation: examples from the elastin-like polypeptide system. *Biomacromolecules* **3**(2), 357–67, Jan (2002).



- [77] Hoover, D. M. and Lubkowski, J. Dnaworks: an automated method for designing oligonucleotides for pcr-based gene synthesis. *Nucleic Acids Res.* **30**(10), e43, May (2002).
- [78] Zhang, K., Diehl, M. R., and Tirrell, D. A. Artificial polypeptide scaffold for protein immobilization. *J. Am. Chem. Soc.* **127**(29), 10136–7, Jul (2005).
- [79] Kuznetsov, S. A. and Gelfand, V. I. Bovine brain kinesin is a microtubule-activated atpase. *Proc. Natl. Acad. Sci. USA* **83**(22), 8530–4, Nov (1986).
- [80] Williams, R. C. and Lee, J. C. Preparation of tubulin from brain. *Meth. Enzymol.* **85 Pt B**, 376–85, Jan (1982).
- [81] Castoldi, M. and Popov, A. V. Purification of brain tubulin through two cycles of polymerization-depolymerization in a high-molarity buffer. *Protein Expr. Purif.* **32**(1), 83–8, Nov (2003).
- [82] Rogers, A. R., Driver, J. W., Constantinou, P. E., Jamison, D. K., and Diehl, M. R. Negative interference dominates collective transport of kinesin motors in the absence of load. *Phys. Chem. Chem. Phys.* **11**(24), 4882–9, Jun (2009).
- [83] Gibbons, I. R. and Fronk, E. A latent adenosine triphosphatase form of dynein 1 from sea urchin sperm flagella. *J. Biol. Chem.* **254**(1), 187–96, Jan (1979).  
Notes: Axoneme Prep protocol.
- [84] Nicastro, D., Schwartz, C., Pierson, J., Gaudette, R., Porter, M. E., and McIntosh, J. R. The molecular architecture of axonemes revealed by cryoelectron tomography. *Science* **313**(5789), 944–8, Aug (2006).

- [85] Vale, R. D., Funatsu, T., Pierce, D. W., Romberg, L., Harada, Y., and Yanagida, T. Direct observation of single kinesin molecules moving along microtubules. *Nature* **380**(6573), 451–3, Apr (1996).
- [86] Koster, G., VanDuijn, M., Hofs, B., and Dogterom, M. Membrane tube formation from giant vesicles by dynamic association of motor proteins. *Proc. Natl. Acad. Sci. USA* **100**(26), 15583–8, Dec (2003).
- [87] Shubeita, G. T., Tran, S. L., Xu, J., Vershinin, M., Cermelli, S., Cotton, S. L., Welte, M. A., and Gross, S. P. Consequences of motor copy number on the intracellular transport of kinesin-1-driven lipid droplets. *Cell* **135**(6), 1098–1107, Dec (2008).
- [88] Bruno, L., Echarte, M. M., and Levi, V. Exchange of microtubule molecular motors during melanosome transport in *xenopus laevis* melanophores is triggered by collisions with intracellular obstacles. *Cell Biochem. Biophys.* **52**(3), 191–201, Jan (2008).
- [89] Yildiz, A., Tomishige, M., Gennerich, A., and Vale, R. D. Intramolecular strain coordinates kinesin stepping behavior along microtubules. *Cell* **134**(6), 1030–41, Sep (2008).
- [90] Blaker, W. D., Goodrum, J. F., and Morell, P. Axonal transport of the mitochondria-specific lipid, diphosphatidylglycerol, in the rat visual system. *J. Cell. Biol.* **89**(3), 579–84, Jun (1981).
- [91] Argyropoulos, G., Stütz, A. M., Ilnytska, O., Rice, T., Teran-Garcia, M., Rao, D. C., Bouchard, C., and Rankinen, T. Kif5b gene sequence variation and

- response of cardiac stroke volume to regular exercise. *Physiol. Genomics* **36**(2), 79–88, Jan (2009).
- [92] Pilling, A. D., Horiuchi, D., Lively, C. M., and Saxton, W. M. Kinesin-1 and dynein are the primary motors for fast transport of mitochondria in drosophila motor axons. *Mol. Biol. Cell* **17**(4), 2057–68, Apr (2006).
- [93] Shimizu, T. and Johnson, K. A. Kinetic evidence for multiple dynein atpase sites. *J. Biol. Chem.* **258**(22), 13841–6, Nov (1983).
- [94] Hirakawa, E., Higuchi, H., and Toyoshima, Y. Y. Processive movement of single 22s dynein molecules occurs only at low atp concentrations. *Proc. Natl. Acad. Sci. USA* **97**(6), 2533–7, Mar (2000).
- [95] Shiroguchi, K. and Toyoshima, Y. Y. Regulation of monomeric dynein activity by atp and adp concentrations. *Cell Motil. Cytoskel.* **49**(4), 189–99, Aug (2001).